



# On discontinuous Galerkin approach for atmospheric flow in the mesoscale with and without moisture

DIETER SCHUSTER<sup>1\*</sup>, SLAVKO BRDAR<sup>1</sup>, MICHAEL BALDAUF<sup>1</sup>, ANDREAS DEDNER<sup>2</sup>, ROBERT KLÖFKORN<sup>3</sup>  
and DIETMAR KRÖNER<sup>4</sup>

<sup>1</sup>Deutscher Wetterdienst, Offenbach, Germany

<sup>2</sup>Mathematics Institute, University of Warwick, Coventry, UK

<sup>3</sup>National Center for Atmospheric Research, Boulder, CO, USA

<sup>4</sup>Section of Applied Mathematics, University of Freiburg, Freiburg i. Br., Germany

(Manuscript received December 16, 2013; in revised form April 22, 2014; accepted June 3, 2014)

## Abstract

We present and discuss discontinuous Galerkin (DG) schemes for dry and moist atmospheric flows in the mesoscale. We derive terrain-following coordinates on the sphere in strong-conservation form, which makes it possible to perform the computation on a Cartesian grid and yet conserves the momentum density on an  $f$ -plane. A new DG model, i.e. DG-COSMO, is compared to the operational model COSMO of the Deutscher Wetterdienst (DWD). A simplified version of the suggested terrain-following coordinates is implemented in DG-COSMO and is compared against the DG dynamical core implemented within the DUNE framework, which uses unstructured grids to capture orography. Finally, a few idealised test cases, including 3d and moisture, are used for validation. In addition an estimate of efficiency for locally adaptive grids is derived for locally and non-locally occurring phenomena.

**Keywords:** dynamical core, discontinuous galerkin, coupling physics

## 1 Introduction

Dynamical cores for weather prediction or climate models, i.e. numerical solvers for the Euler equations or similar models, are increasingly based on finite-volume type discretisations. These schemes have often been mandatory in other areas of fluid dynamic simulations due to their property to locally conserve the prognostic variables and therefore to treat shocks and other discontinuities correctly. However, it is not easy to formulate higher order schemes for these methods in complex geometries using non-cartesian grids. On the other hand, higher order discretisations are relatively easy to achieve with finite-element schemes; however, they are not locally conservative, in general. During recent years discontinuous Galerkin (DG) methods (e.g. COCKBURN and SHU (1989); COCKBURN et al. (1989); COCKBURN et al. (1990)) have become popular in the fluid dynamics community. They combine the ideas of finite-volume and finite-element schemes and consequently promise to be both locally conserving and to allow discretisations of almost arbitrary order. Additional appreciated properties of DG discretisations are compact stencils, which facilitate their implementation on massively parallel computing architectures. Furthermore, it is easy to employ both static or dynamic grid refinements.

Consequently, several groups have started to investigate the DG method for usability in numerical models for the atmosphere. For example, GIRALDO and

RESTELLI (2008) implemented the DG method for three different sets of budget equations and compared them with respect to their conservation properties, accuracy and efficiency. The application of DG to solve shallow water models on the sphere is found in GIRALDO et al. (2002). In NAIR et al. (2009) (see also references therein) DG methods have been successfully considered for hydrostatic global models. The convergence of a global DG model for a scalar advection equation on a Yin-Yang grid is studied in HALL and NAIR (2012).

Other work shows, that variable resolution techniques are becoming more and more relevant in atmospheric flow applications, most notably BEHRENS (2006), but also in JABLONOWSKI et al. (2009) or the MPAS framework by SKAMAROCK et al. (2012) just to name a few. MÜLLER et al. (2013) study an idealised test case of a rising dry bubble, demonstrating that adaptive grid refinement has a considerable potential to reduce computational costs compared with a uniform grid. A similar statement is done by BLAISE and ST-CYR (2012) where an adaptive DG method is considered for the shallow water equations on the sphere.

In contrast to the above mentioned positive properties of DG schemes there are also some unsolved problems, perhaps the most prominent is the relatively small time step (or small Courant number) that has to be used and so far prevents the method from being competitive with currently used dynamical cores. Therefore, there has so far been little effort to go beyond these idealised studies with a dry atmosphere. GABERSEK et al. (2012) presents

\*Corresponding author: Dieter Schuster, Deutscher Wetterdienst, Frankfurter Straße 135, 63067 Offenbach, Germany, e-mail: Dieter.Schuster@dwd.de

besides dry test cases a two-dimensional study of cloud development with rain simulated with a nodal spectral element model using inexact quadrature formulas and semi-implicit time integration. They discuss the dependence on the grid and order refinement. For the dry simulations the solution converges to a reference solution computed on a fine grid. But for the moist simulations the solution changes with refinement. The authors make the hypothesis that the strong non-linearity of the moist equations is responsible for this behaviour.

The new “Non-hydrostatic Unified Model for the Atmosphere” (*NUMA* for short) uses continuous and discontinuous Galerkin methods (e.g. [KELLY and GIRALDO \(2012\)](#)) and is developed at the Naval Postgraduate School and the Naval Research Laboratory by the group around Francis X. Giraldo. In this work we take a different approach and introduce a new dynamical core based on a DG method into an existing model. This approach enables us to carry out a detailed comparison of our new dynamical core with a well established model. We chose the COSMO model which is used for operational weather prediction at the Deutscher Wetterdienst and several other weather services. COSMO is a limited area model and is used for short range predictions. Its current dynamical core solves the non-hydrostatic fully compressible Euler equations in advection form and is based on finite differences. The COSMO model is described by [STEPPELER et al. \(2003\)](#); [BALDAUF et al. \(2011\)](#), a scientific documentation is given in [DOMS et al. \(2011a\)](#); [DOMS et al. \(2011b\)](#), and a short summary in [BRDAR et al. \(2013\)](#).

The new DG based model is described in section 2. It is based on the Euler equations including moisture terms, formulated in strong-conservation form using terrain-following coordinates. In this article we compare the new model, called *DG-COSMO*, with the finite difference solver of COSMO. For a more thorough study of the DG approach, we also include some comparisons with the DG dynamical core implemented in the DUNE framework (see [DEDNER et al. \(2010\)](#) and references therein). This model was compared directly with COSMO in [BRDAR et al. \(2013\)](#). The main conceptual differences between *DG-COSMO* and the DUNE implementation are the coordinate system and grid structure used for the spatial discretization. While *DG-COSMO* uses terrain following coordinates and consequently a structured quadrilateral grid for the spatial discretization, the DUNE model uses  $z$ -coordinates and can handle very general grid structures (structured, semi-structured, or totally unstructured). The general grid structure also allows for the use of local grid refinement and a new refinement indicator has been implemented within the DUNE dynamical core for mesoscale applications (see [BRDAR et al. \(2013\)](#) and [BALDAUF and BRDAR \(2013\)](#)).

Two *DG-COSMO* validation test cases are shown in section 3. These are a two-dimensional mountain overflow and a gravity wave expansion in a channel. General questions, like the choice of basis functions and

the well-balancing problem are also addressed in this section. We make a small comparison between all three models (*COSMO*, *DG-COSMO*, and *DUNE*), focusing on their capturing of orographic features when a dry atmosphere is at rest. As pointed out, *COSMO* and *DG-COSMO* use terrain following coordinates and *DUNE* uses unstructured grids for the orography. Furthermore two popular test cases with local and non-local character are chosen to test the new adaptation criterion. The cold density current [STRAKA et al. \(1993\)](#) is the one with local character where the adaptive mesh refinement (AMR) technique is shown to be more efficient by a factor of 4. Similar results have been achieved in [MÜLLER et al. \(2013\)](#), but with a different refinement criterion. Finally, a three-dimensional moist convection test case without rain in a similar background atmosphere as in [WEISMAN and KLEMP \(1982\)](#) is investigated.

## 2 DG scheme

The starting point for our model are the compressible, non-hydrostatic Euler equations for a moist atmosphere on a rotating sphere written in conservation form

$$\frac{\partial \rho'}{\partial t} + \nabla \cdot \rho \mathbf{u} = 0, \quad (2.1)$$

$$\frac{\partial \rho \mathbf{u}}{\partial t} + \nabla \cdot (\rho \mathbf{u} \otimes \mathbf{u} + p' \mathbf{I}) = -\rho' g \mathbf{k} - 2\rho \boldsymbol{\Omega} \times \mathbf{u}, \quad (2.2)$$

$$\frac{\partial (\rho \theta)'}{\partial t} + \nabla \cdot \rho \theta \mathbf{u} = s_\theta, \quad (2.3)$$

in which  $\otimes$  is the dyadic product,  $\mathbf{I}$  is the unit matrix, and  $\mathbf{k}$  is the vertical unit base vector.  $s_\theta$  is the source term of the temperature equation, which is equal to zero for a dry atmosphere. To reduce discretisation errors, e.g. by the use of terrain-following coordinates, the thermodynamic variables density  $\rho = \rho_0 + \rho'$ , pressure  $p = p_0 + p'$ , and potential temperature  $\theta = \theta_0 + \theta'$  are split into a reference state (lower index ‘0’) and deviations (denoted by ‘’). The reference state fulfils the dry ideal gas law  $p_0 = R_d \rho_0 T_0$  and the hydrostatic equation  $\nabla p_0 = -g \rho_0 \mathbf{k}$  where  $R_d = 287.05 \frac{\text{J}}{\text{kg}\cdot\text{K}}$  is the gas constant of dry air and  $g = 9.80665 \frac{\text{m}}{\text{s}^2}$  is the absolute value of acceleration due to gravity. One thermodynamic field can be arbitrarily chosen; here, we prescribe a temperature profile of the form

$$T_0(z) = T_{\text{str}} + (T_{\text{sl}} - T_{\text{str}}) \exp\left(-\frac{z}{H_{\text{scal}}}\right) \quad (2.4)$$

with  $T_{\text{sl}} = 288.15 \text{ K}$ ,  $T_{\text{str}} = 213.15 \text{ K}$  and  $H_{\text{scal}} = 10 \text{ km}$  (e.g. [ZÄNGL \(2012\)](#)).

In the case of *DG-COSMO*, the equations are formulated in terrain-following coordinates  $(\lambda, \phi, \zeta(\lambda, \phi, r))$  on the sphere. The momentum equations (2.2) in strong-

conservation form are

$$\begin{aligned} & \frac{\partial \sqrt{G'} \rho u}{\partial t} + \frac{\partial}{\partial \lambda} \left( \sqrt{G'} \frac{\rho u u + p'}{r \cos \phi} \right) + \frac{\partial}{\partial \phi} \left( \sqrt{G'} \frac{\rho u v}{r} \right) \\ & + \frac{\partial}{\partial \zeta} \left( \sqrt{G'} \left[ \frac{\partial \zeta}{\partial \lambda} \frac{\rho u u + p'}{r \cos \phi} + \frac{\partial \zeta}{\partial \phi} \frac{\rho u v}{r} + \frac{\partial \zeta}{\partial z} \rho u w \right] \right) \\ & = \sqrt{G'} (S^{*\lambda} - b^{*\lambda}), \end{aligned} \quad (2.5)$$

$$\begin{aligned} & \frac{\partial \sqrt{G'} \rho v}{\partial t} + \frac{\partial}{\partial \lambda} \left( \sqrt{G'} \frac{\rho v u}{r \cos \phi} \right) + \frac{\partial}{\partial \phi} \left( \sqrt{G'} \frac{\rho v v + p'}{r} \right) \\ & + \frac{\partial}{\partial \zeta} \left( \sqrt{G'} \left[ \frac{\partial \zeta}{\partial \lambda} \frac{\rho v u}{r \cos \phi} + \frac{\partial \zeta}{\partial \phi} \frac{\rho v v + p'}{r} + \frac{\partial \zeta}{\partial z} \rho v w \right] \right) \\ & = \sqrt{G'} (S^{*\phi} - b^{*\phi}), \end{aligned} \quad (2.6)$$

$$\begin{aligned} & \frac{\partial \sqrt{G'} \rho w}{\partial t} + \frac{\partial}{\partial \lambda} \left( \sqrt{G'} \frac{\rho w u}{r \cos \phi} \right) + \frac{\partial}{\partial \phi} \left( \sqrt{G'} \frac{\rho w v}{r} \right) \\ & + \frac{\partial}{\partial \zeta} \left( \sqrt{G'} \left[ \frac{\partial \zeta}{\partial \lambda} \frac{\rho w u}{r \cos \phi} + \frac{\partial \zeta}{\partial \phi} \frac{\rho w v}{r} \right. \right. \\ & \left. \left. + \frac{\partial \zeta}{\partial z} (\rho w w + p') \right] \right) \\ & = \sqrt{G'} (S^{*z} - b^{*z}), \end{aligned} \quad (2.7)$$

with the metric correction terms

$$\begin{aligned} b^{*\lambda} &= -\frac{1}{r} \rho u w + \frac{\tan \phi}{r} \rho u v, \\ b^{*\phi} &= -\frac{1}{r} \rho v w + \frac{\tan \phi}{r} (\rho u^2 + p'), \\ b^{*z} &= -\frac{1}{r} (\rho (u^2 + v^2) + 2p'). \end{aligned} \quad (2.8)$$

and the physical components for the source term are

$$\begin{aligned} S^{*\lambda} &= 2\rho\Omega (v \sin \phi - w \cos \phi), \\ S^{*\phi} &= -2\rho\Omega u \sin \phi, \\ S^{*z} &= -\rho'g + 2\rho\Omega u \cos \phi. \end{aligned} \quad (2.9)$$

The derivation of these equations and the notations are given in appendix 6. In particular,  $\sqrt{G'}$  is given by Eq. (A.21). The analogous form for the scalar equations is given by (A.23).

For the moist atmosphere we use additional quantities for the mass fraction of water vapour  $q_v$  and cloud water  $q_c$  with their budget equations

$$\frac{\partial \rho q_x}{\partial t} + \nabla \cdot \rho q_x \mathbf{u} = s_x, \quad x \in \{v, c\}. \quad (2.10)$$

COSMO makes the assumption that the specific heat capacity  $c_{pml}$  of moist air is equal to that of dry air (see Doms et al. (2011a)). The same assumption is made for DG-COSMO. This means that in equation (2.1) we use instead of the potential temperature the approximated

moist potential temperature  $\theta_m$

$$\theta_m = \frac{R_m}{R_d} T \left( \frac{p_{00}}{p} \right)^{\frac{R_m}{c_{pd}}}$$

which is a conserved variable when no phase change happens (see. BRDAR (2012)) and is up to the factor  $\frac{R_m}{R_d}$  and the approximation  $c_{pml} = c_{pd} = 1005 \frac{J}{kg \cdot K}$  identical to the definition in BRYAN and FRITSCH (2002). With the gas constant of water vapour  $R_v = 461.51 \frac{J}{kg \cdot K}$  the moist gas constant is defined as

$$R_m = (1 - q_v - q_c)R_d + q_v R_v.$$

The source terms  $s_v$ ,  $s_c$  and  $s_\theta$  describe the phase change of water and the released or absorbed latent heat. The equation of state including moisture is

$$p = p_{00} \left( \frac{R_d}{p_{00}} \rho \theta_m \right)^{\frac{c_{pd}}{c_{vml}}},$$

where  $c_{vml} = c_{pd} - R_m$ . For the dry case  $c_{vml}$  reduces to the dry specific heat capacity  $c_{vd}$  and  $\theta_m$  to  $\theta$ , respectively. As usual, we fix  $p_{00} = 10^5$  Pa.

Since the atmosphere is mainly turbulent, Reynolds-averaged Euler equations are usually considered. The turbulent diffusion coefficients are several orders of magnitude larger than the viscous ones, therefore the latter can be neglected. The turbulent fluxes of momentum and heat are described by turbulence parameterizations, i.e. by adding a term  $\nabla \cdot \tau$  to the right hand side of the momentum equation (2.2) with the turbulent stress tensor

$$\tau = \rho \mu_m (\nabla \mathbf{u} + (\nabla \mathbf{u})^T)$$

and the divergence of a turbulent heat flux term of the form

$$\rho \mu_h \nabla \theta$$

to the potential temperature equation (2.3). In this paper we consider only idealised test cases with a prescribed constant viscosity  $\mu_m$  and diffusivity  $\mu_h$  instead of an advanced turbulence model. In this turbulence model the kinetic energy dissipation  $\nabla \cdot (\mathbf{u} \cdot \tau)$  is ignored like in COSMO (see Doms et al. (2011a)). So we use the following equations if diffusion is contained

$$\frac{\partial \rho \mathbf{u}}{\partial t} + \nabla \cdot (\rho \mathbf{u} \otimes \mathbf{u} + p' \mathbf{I} - \tau) = -\rho' g \mathbf{k} - 2\rho \Omega \times \mathbf{u}, \quad (2.11)$$

$$\frac{\partial (\rho \theta)'}{\partial t} + \nabla \cdot (\rho \theta \mathbf{u} - \rho \mu_h \nabla \theta) = s_\theta, \quad (2.12)$$

$$\frac{\partial \rho q_x}{\partial t} + \nabla \cdot (\rho q_x \mathbf{u} - \rho \mu_h \nabla q_x) = s_x, \quad (2.13)$$

where  $x \in \{v, c\}$  and where the diffusion parametrisation for the tracers is in analogy to the potential temperature with the same diffusion coefficients. These are

the same equations as equation set 2 in GIRALDO and RESTELLI (2008), but with a symmetric viscous stress tensor. For the formulation of these equations in the strong-conservation form we refer to BALDAUF (2005).

### Spatial discretisation

Since the discretisation used in COSMO and within the DUNE framework have been discussed briefly in BRDAR et al. (2013), and in the references provided there, we focus here on describing the approach used within DG-COSMO. The equation system (2.1)–(2.3) and (2.10) or their terrain-following transformed counterparts can be written in the compact form

$$\frac{\partial \mathbf{q}}{\partial t} + \nabla \cdot \mathbf{F}(\mathbf{q}) = \mathbf{S}(\mathbf{q}). \quad (2.14)$$

Let the computational domain be  $\Omega$  and consider a tessellation  $\Omega_1, \dots, \Omega_N$  of quadrilateral elements of  $\Omega$ . In physical space, these elements usually are vertically stretched and are horizontally slightly deformed due to the convergence of the spherical coordinates towards the poles. We use the same vertical stretching as in BALDAUF (2013a), p. 33. Let  $H$  be the height of the domain and let  $z_k$  be the height in the Cartesian grid of the vertical faces between the elements, with  $z_1 = H$  and  $z_{K+1} = 0$ , then  $z_k$  is computed by

$$\begin{aligned} z_k &= H(\beta \eta_k^2 + (1 - \beta) \eta_k), \\ \eta_k &= 1 - \frac{k-1}{K}, \quad k = 1, \dots, K+1, \end{aligned} \quad (2.15)$$

with a stretching factor  $\beta$ . The discretisation  $\mathbf{q}_h$  of the prognostic variables  $\mathbf{q}$  restricted to an element  $\Omega_i$ ,  $i \in \{1, \dots, N\}$  is a polynomial  $\mathbf{q}_i$

$$\mathbf{q}_{h|\Omega_i}(t, \mathbf{x}) = \mathbf{q}_i(t, \mathbf{x}) = \sum_{l=1}^d q_{i,l}(t) \varphi_l(\xi(\mathbf{x} - \mathbf{x}_i)), \quad (2.16)$$

where  $\mathbf{x}_i$  is the center of each cell and  $\xi$  maps the interval  $([-\frac{\Delta\lambda}{2}, \frac{\Delta\lambda}{2}], [-\frac{\Delta\phi}{2}, \frac{\Delta\phi}{2}], [-\frac{\Delta\zeta}{2}, \frac{\Delta\zeta}{2}])$  into the interval  $[-1, 1]^{\dim\Omega}$ .  $\mathcal{B} := \{\varphi_1(\xi), \dots, \varphi_d(\xi)\}$  is a  $d$ -dimensional basis of the discretised solution space. In the discontinuous Galerkin approach we multiply (2.14) for each element  $\Omega_i$  with a test function  $\varphi_m$  and integrate over that element. After integration by parts of the divergence term and the replacement of  $\mathbf{q}_{|\Omega_i}$  with the discretisation  $\mathbf{q}_i$  we arrive at

$$\begin{aligned} \sum_{l=1}^d \frac{dq_{i,l}}{dt} \int_{\Omega_i} \varphi_l \varphi_m d\Omega &= - \int_{S=\partial\Omega_i} \mathbf{F}(\mathbf{q}_h) \cdot \mathbf{n} \varphi_m dS \\ &+ \int_{\Omega_i} \mathbf{F}(\mathbf{q}_i) \cdot \nabla \varphi_m d\Omega + \int_{\Omega_i} \mathbf{S}(\mathbf{q}_i) \varphi_m d\Omega, \end{aligned} \quad (2.17)$$

for  $i \in \{1, \dots, N\}$ .  $\mathbf{n}$  is the outward directed unit vector normal on  $\partial\Omega_i$ . The integral on the left side corresponds to the mass matrix  $\mathbf{M}_{lm}$  on the single element  $\Omega_i$ . We

search for a function  $\mathbf{q}$  that fulfils (2.17) for all  $\varphi_m \in \mathcal{B}$  on all elements. Between the elements the solution can be discontinuous, so we need to replace the physical flux  $\mathbf{F}(\mathbf{q}_h) \cdot \mathbf{n}$  with a numerical flux function  $(\mathbf{F}(\mathbf{q}_h) \cdot \mathbf{n})^*$  to get a well defined scheme. Usually, the Rusanov flux is taken

$$(\mathbf{F}(\mathbf{q}_h) \cdot \mathbf{n})^*_{|e} := \frac{1}{2}(\mathbf{F}(\mathbf{q}_i) + \mathbf{F}(\mathbf{q}_j)) \cdot \mathbf{n}_{|e} - \frac{1}{2}\lambda(\mathbf{q}_j - \mathbf{q}_i)$$

where  $e = \Omega_i \cap \Omega_j$  and  $\lambda = \max_e(c + \sqrt{\mathbf{u} \cdot \mathbf{n}})$  is the speed of the fastest permissible wave.  $c$  is the speed of sound given by  $c^2 = \frac{c_{pd}}{c_{vd}} R_d T$ . Lobatto-Gauß-Legendre quadrature formulas are used for numerical integration (see GASSNER (2009) for a discussion on quadrature formulas). For the basis  $\mathcal{B}$ , we either choose the full tensor product of Legendre polynomials  $\mathcal{B}_{fp}$  up to a chosen degree  $\kappa$ , or a minimal basis of products of Legendre polynomials  $\mathcal{B}_{mb}$  where the total degree is bounded by  $\kappa$ , i.e.

$$\begin{aligned} \mathcal{B}_{fp} &= \left\{ b(\xi) \left| b = \prod_{i=1}^{\dim\Omega} P_{l_i}(\xi_i), l_i \leq \kappa \right. \right\}, \\ \mathcal{B}_{mb} &= \left\{ b(\xi) \left| b = \prod_{i=1}^{\dim\Omega} P_{l_i}(\xi_i), \sum_{i=1}^{\dim\Omega} l_i \leq \kappa \right. \right\}, \end{aligned}$$

where  $P_l$  is the  $l$ -th normalised Legendre polynomial. Choosing the Legendre polynomials is known as the modal approach and results in a diagonal mass matrix for the system (2.17). Consequently, there is no direct physical interpretation of the coefficients  $q_{i,l}$  in (2.16).

In order to discretise equations (2.11)–(2.13), we use the local discontinuous Galerkin (LDG) scheme (e.g. COCKBURN and SHU (1998)) which is known to be of the  $\kappa + 1$  spatial accuracy order when the polynomials up to the  $\kappa$ -th degree are used for the basis. Here, we describe the scheme just for (2.11), because the scalar case is analogous. We split the equation (2.11) into a system of two coupled equations with only first order derivatives introducing an auxiliary variable  $\mathbf{V}$

$$\begin{aligned} \frac{\partial \rho \mathbf{u}}{\partial t} + \nabla \cdot (\rho \mathbf{u} \otimes \mathbf{u} + p' \mathbf{I} - \rho \mu (\mathbf{V} + \mathbf{V}^T)) \\ = -\rho' g \mathbf{k} - 2\rho \Omega \times \mathbf{u}, \end{aligned} \quad (2.18)$$

$$\nabla \mathbf{u} = \mathbf{V}. \quad (2.19)$$

At first, the equation (2.18) is handled by the Galerkin approach, i.e. it is multiplied with a test function and integrated over an element  $\Omega_i$ . After integration by parts of the left side and the replacement of the flux in the integral over the element face with a numerical flux, equation (2.18) becomes

$$\int_{S=\partial\Omega_i} (\mathbf{u} \cdot \mathbf{n})^* \varphi dS - \int_{\Omega_i} \mathbf{u} \nabla \varphi d\Omega_i = \int_{\Omega_i} \mathbf{V} \varphi d\Omega_i.$$

The LDG scheme solves this last equation for  $\mathbf{V}$ . In the second step  $\mathbf{V}$  is inserted into (2.18) and the DG scheme for the advection equation described above is applied.

The diffusive numerical flux  $(\mathbf{u} \cdot \mathbf{n})^*_e$  for  $e = \Omega_i \cap \Omega_j$  is given as

$$(\mathbf{u} \cdot \mathbf{n})^*_e := \frac{1}{2}(\mathbf{u}_i + \mathbf{u}_j) \cdot \mathbf{n}.$$

We choose free slip boundary conditions for the velocity on all non-periodic and non-open boundaries, i.e.  $\mathbf{u} \cdot \mathbf{n} = 0$ ,  $\nabla \mathbf{u} \cdot \mathbf{n} = 0$  and additionally  $\frac{\partial \theta}{\partial z} = 0$  on the vertical boundaries and  $\frac{\partial \theta}{\partial x} = 0$  horizontally.

### Time discretisation

Equation system (2.17) is a system of nonlinear ODEs of the form

$$\frac{d}{dt} \mathbf{q}_h(t) = \mathbf{M}^{-1} \mathcal{L}(t, \mathbf{q}_h).$$

where the operator  $\mathcal{L}$  is given by the rhs. of Eq. (2.17). Given an initial condition  $\mathbf{q}(t = 0) = \mathbf{q}_{\text{init}}$  and an end time  $t_{\text{end}} > 0$ , we apply general explicit  $m$ -stage Runge-Kutta time integration schemes of the form

$$\begin{aligned} \mathbf{q}_h^{n+1} &= \mathbf{q}_h^n + \Delta t \sum_{l=1}^m b_l \mathbf{h}_l, \quad \mathbf{q}_h^0 = \mathbf{q}_{h,\text{init}}, \\ \mathbf{h}_l &= \mathbf{M}^{-1} \mathcal{L} \left( t^n + \Delta t c_l, \mathbf{q}_h^n + \Delta t \sum_{r=1}^{l-1} a_{lr} \mathbf{h}_r \right), \end{aligned}$$

for  $l = 1, \dots, m$ ,  $n = 0, \dots, \lfloor t_{\text{end}}/\Delta t \rfloor$  under the consistency condition  $\sum_{l=1}^m b_l = 1$  and the autonomous condition  $c_l = \sum_{r=1}^m a_{lr}$ . Coefficients  $a_{lr}$ ,  $b_l$ , and  $c_l$  are further more determined so that the order of the  $m$ -stage Runge-Kutta scheme is equal to the order of the discontinuous Galerkin scheme.

The source terms  $s_v$ ,  $s_c$  and  $s_\theta$  are handled through a process splitting. We distinguish two time steps, one for the advection (or the DG scheme)  $\Delta t$  and one for the phase change  $\Delta \tau$  with  $\Delta \tau = \sigma \Delta t$  for an integer  $\sigma$ . First the advective terms are integrated with the Runge-Kutta scheme described above with  $\Delta t$  for  $\sigma$  steps, then a saturation adjustment on each quadrature point results in new tendencies for the source terms of the phase change. These tendencies are kept constant for the next  $\sigma$  advection time steps. The size of the integer  $\sigma$  is determined by experiments (see section 3.5). The saturation adjustment reduces an oversaturation of water vapour to saturation by condensation. Cloud water in an undersaturated air parcel is evaporated until all cloud water is evaporated or saturation is reached. The absolute temperature  $T$  is adjusted accordingly. DG-COSMO uses an *isochoric* saturation adjustment, whereas COSMO until now uses a similar *isobaric* scheme (DOMS et al. (2011b)). Note that under the assumption  $c_{pml} = c_{pd}$ , our saturation adjustment is identical to the one by TOMITA (2008). Saturation adjustment assumes that the phase change is infinitely fast, so the model does not need a parameter for the time scale. We note, that the analogous phase change parametrisation in DUNE is modelled by

a simple analytic evaporation function containing a relaxation time scale (see BRDAR (2012)). However, due to the above mentioned time-splitting, the time scale  $\Delta \tau$  has a similar effect. If the time scale is chosen too large, the oversaturation will decrease too slowly, and as a result the convection is slowed down as well. Similar observations are made in DG-COSMO (see section 3.5 and Fig. 10). The saturation adjustment in the DG context is first applied in the quadrature points. If operator splitting is used a projection to the modal coefficients  $\mathbf{q}_{i,l}$  in (2.16) is needed. To avoid this additional projection for every saturation adjustment, we decided to use process splitting in DG-COSMO, because in this case we can use the adjusted values in the quadrature points directly.

There are a few drawbacks of the current state of DG-COSMO that we want to mention. One is the lack of positivity preservation. In the saturation adjustment we clip all negative values of  $q_v$  and  $q_c$  to zero like in GABERSEK et al. (2012), and therefore we lose the mass conservation for moist atmospheres. A further technical aspect is, that DG-COSMO uses the same output routines as COSMO, so just one point per element can be written, plotted and post-processed.

### Adaptive grid refinement

The vast spectrum of atmospheric spatial and temporal scales makes adaptive mesh refinement (AMR) an interesting numerical technique. In contrast to the finite difference scheme, the use of AMR is intrinsic to the discontinuous Galerkin or finite volume scheme, and requires no significant change to the numerical model other than simple prolongation and restriction of the data between coarse and fine mesh cells. The prolongation and restriction process is carried out in such an intuitive manner, that the mass and the density potential temperature  $\rho \theta$  are preserved within the refined or coarsened cells. Most notably, the AMR has been deployed in the operational model OMEGA (see BOYBEYI et al. (2001); BACON et al. (1999); GOPALAKRISHNAN et al. (2002)) for extreme weather prediction.

Dynamical AMR requires an indicator which decides whether a mesh cell  $\Omega_i$  should be refined or coarsened. In our case, the indicator is the maximal jump  $\eta_i$  of potential temperature between the neighbouring cells, relative to the maximal jump  $\eta_{\text{max}}$  over the whole grid. Thus, we take

$$\begin{aligned} \eta_i &= \max_{\Omega \in \mathcal{N}(\Omega_i)} \eta(\Omega_i, \Omega) \cdot \eta_{\text{max}}^{-1}, \\ \eta(\Omega_i, \Omega) &= \max_{\substack{a \in \mathcal{Q}(\Omega_i) \\ b \in \mathcal{Q}(\Omega)}} |\theta'(b) - \theta'(a)|, \\ \eta_{\text{max}} &= \max_{i,j} \{ \eta(\Omega_i, \Omega_j) \mid \Omega_j \in \mathcal{N}(\Omega_i) \}, \end{aligned}$$

where  $\mathcal{N}(\Omega_i)$  is the family of all mesh elements neighbouring  $\Omega_i$ .  $\mathcal{Q}(\Omega_i)$  is the set of quadrature points which allow exact numerical integration of polynomial on  $\Omega_i$ .

of degree up to the order of the discontinuous Galerkin scheme, however not larger than third degree. In this way the computational cost for the indicator, computed every 5th DG time step, is reduced with negligible impact to the indicator values. A simple rule can be stated, if  $\eta_i > \frac{1}{10}$  then  $\Omega_i$  will be refined, otherwise if  $\eta_i < \frac{1}{100}$ , an attempt to remove  $\Omega_i$  together with correspondingly marked cells belonging to the same father element is carried out. The two threshold values are chosen based on several trial-and-error tests until satisfactory results with respect to the error and computational time are reached. This kind of approach can, however, lead to infinite refinement of cells close to an oscillation in the numerical solution. To prohibit this, we assign to each cell a refinement level – a nonnegative integer which is zero for all cells in the start mesh, and increases by 1 when a cell is refined, or decreases by 1 when coarsened. The maximal refinement level is then set to control AMR. Also only elements with positive refinement level can be coarsened. To keep track which elements were created from which father element, we use a *hierarchical* grid structure (see KLÖFKORN (2009)) so that coarsening is an exactly reversible operation to grid refinement.

### 3 Numerical results

In this section we present six test cases. The first two are used to validate the new DG-COSMO core: the gravity wave in a channel described by BALDAUF and BRDAR (2013) and a linear hydrostatic mountain overflow as in DURRAN and KLEMP (1983). After this validation, an atmosphere at rest with a mountain in the middle of the domain is simulated to investigate the well-balancing properties of the three solvers (COSMO, DG-COSMO, and DUNE) with their different discretization approaches and different grid structures. To test dynamic grid adaptation, we choose one test case with locally occurring and one with non-locally evolving phenomena, e.g. STRAKA et al. (1993) and SKAMAROCK and KLEMP (1994). Finally, we study the implemented moist physics on a rising moist bubble.

Given a reference solution  $\psi_{\text{ref}}$ , the error in the quantity  $\psi$  is computed in a relatively large domain  $\Omega_L \subset \Omega$ , containing a fixed number  $N$  of grid elements, by evaluating the deviations  $|\psi - \psi_{\text{ref}}|$  at the midpoints of all elements. The  $L_h$ -error in  $\Omega_L$  is then defined as

$$L_h = \sqrt{\frac{1}{\|\Omega_L\|} \sum_{i=1}^N |\psi_i - \psi_{\text{ref},i}|^h \cdot \|\Omega_i\|}. \quad (3.1)$$

If not stated otherwise,  $\Omega_L$  is the full computational domain  $\Omega$ . In addition, to that, with the DUNE core, we can take arbitrary  $N$  equally sized elements to compute  $L_h$ . If there is a known (linearised) analytic solution, we will take this as reference. Otherwise, we compare the solutions of the different models to each other or with results from the literature. We compare the two basis sets available in the DG implementations on the same

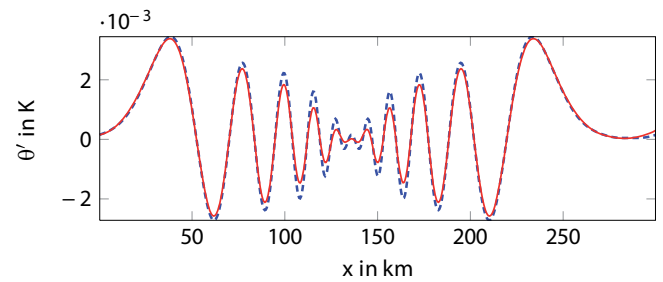


**Figure 1:** Gravity wave expansion in a channel with DG-COSMO. The graph shows a cross section of  $\theta'$  at  $z = 5$  km for the gravity wave test case of BALDAUF and BRDAR (2013) for  $\kappa = 1$  with a grid size of  $\Delta x \times \Delta z = 1000 \text{ m} \times 500 \text{ m}$  after 30 min. The blue dashed line is the analytic linearised solution, the red solid line is the DG-COSMO solution.

grid, and the different models with respect to the same number of degrees of freedom. All three schemes use the same number of degrees of freedom per quantity, so we denote with “DoFs” the number used for a single quantity, in the following.

#### 3.1 Gravity wave in a channel

A first validation is performed with the gravity wave expansion described in BALDAUF and BRDAR (2013). Here we present just the case without Coriolis force, because this force is not implemented in DG-COSMO at the moment. For the test with Coriolis force with the DUNE library we refer to BALDAUF and BRDAR (2013). A temperature perturbation is placed in a two-dimensional channel of 300 km length and 10 km height. The atmosphere around the bubble is hydrostatically balanced, isothermal with  $T_0 = 250 \text{ K}$ , and has a horizontal background flow of  $u_0 = 20 \frac{\text{m}}{\text{s}}$ . This test case is a modification of the well known inertia gravity wave test case of SKAMAROCK and KLEMP (1994). For this modification an analytic solution for the linearised, *compressible* equations is given in BALDAUF and BRDAR (2013). This solution can serve as a reference, provided the amplitude  $\Delta T$  of the perturbation is sufficiently small. Fig. 1 shows  $\theta'$  after 30 min at  $z = 5$  km for a rather coarse grid and  $\kappa = 1$ . The phase speed is well represented by DG-COSMO, but on this grid and due to the low order there is a significant damping. When using an increased order or a refined grid there is no visible damping and the DG-COSMO solution lies on the analytic linearised solution (not shown). Table 1 and Fig. 2 shows the development of the error under grid refinement compared to the linearised analytical solution. For  $\kappa = 2$  the amplitude of the perturbation is taken as 0.001 K and for  $\kappa = 1$  the amplitude 0.01 K is sufficient to show the convergence. So DG-COSMO has the expected convergence order and we conclude that the implementation is correct.

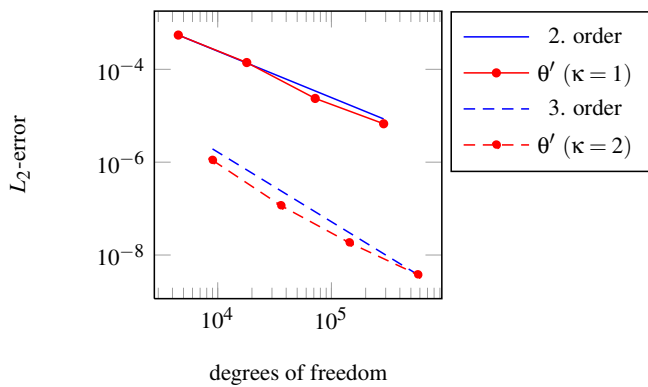
We have compared the full tensor product basis and the minimal basis for the same test case using 8 cores (IBM Power7, 3.84 GHz, 256 kiB L2, 4 MiB L3), with

**Table 1:** Convergence for  $\theta'$  under grid refinement for  $\kappa = 1$  and  $\Delta z = \frac{1}{2}\Delta x$ . The reference is the linearised solution. Subtable (a) shows  $\kappa = 1$  ( $\Delta T = 0.01$  K for reference amplitude) and subtable (b) shows  $\kappa = 2$  ( $\Delta T = 0.001$  K for reference amplitude).

(a) $\kappa = 1$				
grid ( $\Delta x$ )	2000 m	1000 m	500 m	250 m
$L_2$ -error	5.47e-4	1.40e-4	2.36e-5	6.72e-6
EOC	–	1.97	2.57	1.81
$L_\infty$ -error	1.84e-3	5.82e-4	1.02e-4	3.94e-5
EOC	–	1.66	2.52	1.37

(b) $\kappa = 2$				
grid ( $\Delta x$ )	2000 m	1000 m	500 m	250 m
$L_2$ -error	1.09e-6	1.26e-7	1.82e-8	3.77e-09
EOC	–	3.11	2.79	2.27
$L_\infty$ -error	1.34e-5	1.80e-6	2.28e-7	2.21e-08
EOC	–	2.90	2.98	3.37



**Figure 2:** Convergence analysis of DG-COSMO. The graph shows the  $L_2$ -error for the gravity wave test case of BALDAUF and BRDAR (2013) for a second order scheme. The blue line is the idealised  $L_2$ -error and the red line is the  $L_2$ -error  $\theta'$  of the DG-COSMO solution. For 2nd order the lines are solid for 3rd order the lines are dashed.

$\kappa = 3$ ,  $\Delta x = 1$  km and  $\Delta t = 0.125$  s. Table 2 shows, that the minimal basis is significantly faster than the full tensor product while the error is just slightly larger for the minimal basis for this test case.

### 3.1.1 Well-balancing problem

To examine the order needed for the DG scheme, we discuss the well-balancing problem. If the order of the scheme is too low,  $\kappa = 1$  for example, and the reference atmosphere is not the background atmosphere, a spurious deviation from the background of significant size will develop. There are two reasons for this balancing problem. The first is the different numerical treatment in (2.2) of the divergence term and the gravity term on the right hand side. Therefore the numerical errors do not cancel each other resulting in a numerically not balanced scheme. To understand the second independent reason we look at results from a simulation with  $\kappa = 1$ , grid resolution  $\Delta x = 500$  m and time step  $\Delta t = 0.2$  s in Fig. 3. It shows the spurious  $\theta'$  and  $w$  after one single DG time step for a vertical line in the domain at

**Table 2:** Comparison of the error of the full tensor product  $\mathcal{B}_{fp}$  and the minimal basis  $\mathcal{B}_{mb}$ . The relative deviation of the minimal basis is noted in parentheses.

	$\mathcal{B}_{fp}$	$\mathcal{B}_{mb}$	
$L_1$ -error	3.17e-5	3.21e-5	(+1.3%)
$L_2$ -error	4.10e-5	4.18e-5	(+2.0%)
$L_\infty$ -error	1.73e-4	1.76e-4	(+1.7%)
runtime	1 129 s	740 s	1.52 speedup

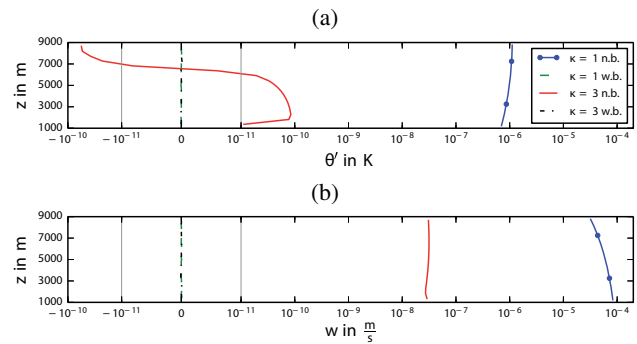


**Figure 3:** The graph shows the well balanced ( $\kappa = 1$  is green dashed,  $\kappa = 3$  is black dashed dot) and the not balanced ( $\kappa = 1$  is blue solid with dots,  $\kappa = 3$  is red solid) solution after one advection time step for a vertical cross cut at  $x = 275$  km. Subfigure (a) shows  $\theta'$  and (b)  $w$ . The abscissa is between  $-10^{-11}$  and  $10^{-11}$  linear, otherwise logarithmic.

$x = 275$  km. This is far away from the bubble. If the reference atmosphere (2.4) is chosen, a significant error is observed over the whole height of the domain, but if the background atmosphere is chosen as reference atmosphere, we see an undisturbed solution. The reason is the vertical component of the Rusanov flux for  $\theta'$ . Let  $\Omega_j$  be the element above  $\Omega_i$  and  $e = \Omega_i \cap \Omega_j$ . We are interested in the flux from  $\Omega_i$  to  $\Omega_j$ , i.e. in the term

$$\frac{1}{2}(\rho\theta_i w_i|_e + \rho\theta_j w_j|_e) - \frac{1}{2}\lambda(\rho\theta'_j|_e - \rho\theta'_i|_e). \quad (3.2)$$

Now we regard the two different reference atmospheres: 1)  $\theta_0$  is the potential temperature of the background atmosphere, in which case the second term of (3.2) vanishes; and 2)  $\theta_0$  is not the background atmosphere, but (2.4) is. While the first term of (3.2) still gives a reasonable discretisation of  $\rho\theta$ , the second term introduces spurious diffusion needed to stabilise the DG scheme, but in this case it also leads to a disturbance in the solution. As shown for  $\kappa = 3$  in Fig. 3 the spurious deviation decreases by a few order of magnitudes. The reason for this is the decreasing size of the jump  $(\rho\theta'_j|_e - \rho\theta'_i|_e)$  caused by the increase in the order of the polynomials. Therefore the diffusion becomes smaller. We conclude that the well-balancing problem becomes less important with increasing order of the scheme.

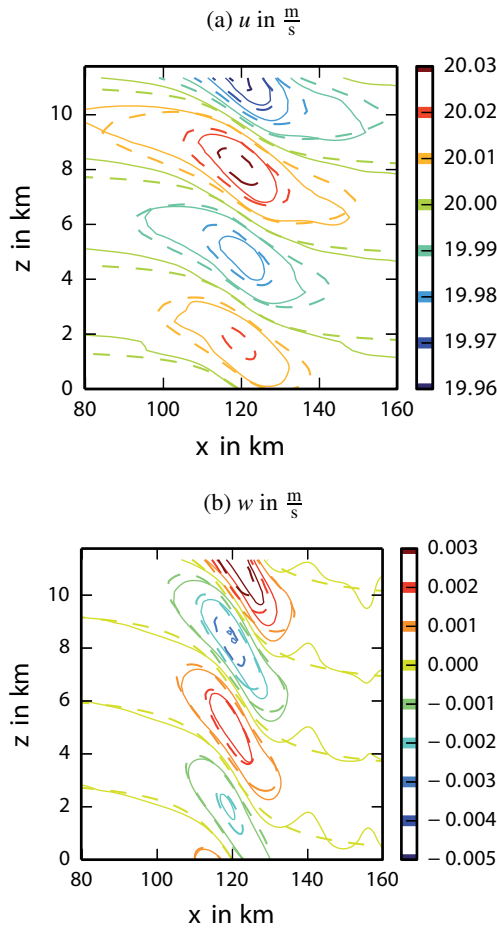


**Figure 4:** Mountain overflow over a mountain with 1 m height and 10 km halfwidth. Subfigure (a) shows the horizontal velocity and (b) the vertical velocity. The solid lines are the DG solution, the dashed lines are the analytic linearised solution.

### 3.2 Mountain overflow

As the second validation test we simulate the two-dimensional flow over a single mountain presented by [DURRAN and KLEMP \(1983\)](#). The mountain height  $z_s$  has the shape of the “versiera di Agnesi”

$$z_s(x) = \frac{h_c}{1 + \left(\frac{x-x_c}{a_c}\right)^2}.$$

The height of the mountain is  $h_c = 1$  m, the half width is  $a_c = 10$  km and the mountain is centred at  $x_c = 120$  km. The initial horizontal wind is  $u_0 = 20 \frac{\text{m}}{\text{s}}$  and the integration time is 20 h. The domain is  $[0, 240 \text{ km}] \times [0, 42 \text{ km}]$  and is partitioned into a grid with  $800 \times 100$  elements. For the vertical grid formula, we use (2.15) with  $\beta = 0.9$ . This results in vertical layers of thickness between 45 m and 795 m in the transformed system. We choose a third order scheme, i.e.  $\kappa = 2$ . The upper 12 km are a sponge layer. Fig. 4 shows the horizontal and vertical wind compared to the analytic linearised solution described in [DURRAN and KLEMP \(1983\)](#) for the lower 12 km.

We also compare the two different basis on the same

**Table 3:** Comparison of the full tensor product and the minimal basis for the mountain wave overflow. The table shows  $w$ , the linearised analytic solution of [DURRAN and KLEMP \(1983\)](#) is taken as reference. The relative deviation of the minimal basis w.r.t the full tensor product is noted in parentheses. The runtime refers to 32 nodes of the Cray XC30 at DWD.

	$\mathcal{B}_{fp}$	$\mathcal{B}_{mb}$	
$L_1$ -error	1.40e-4	1.39e-4	(-0.7 %)
$L_2$ -error	2.21e-4	2.20e-4	(-0.4 %)
$L_\infty$ -error	8.24e-4	8.25e-4	( 0.1 %)
runtime	13 336 s	11 304 s	1.18 speedup

grid for the setup described above. The result for  $w$  in the domain  $\Omega_L = [80 \text{ km}, 160 \text{ km}] \times [0 \text{ km}, 12 \text{ km}]$  is shown in Table 3. Although the full tensor basis has more DoFs than the minimal basis, the overall solution is not more accurate. Thus, it seems that the minimal basis is a more suitable choice for terrain following coordinates.

### 3.3 Atmosphere at rest with a steep mountain

For terrain with steep slopes, the terrain-following coordinate approach produces errors even for an atmosphere at rest. This is even true for numerical models utilising unstructured grids to handle orography. In the following, we will compare the errors of the original COSMO model and the new DG-COSMO core, both using terrain following coordinates, and the DUNE core which captures the orography using unstructured grids. We choose nearly the same setup as described in [ZÄNGL \(2012\)](#). This means that: 1. the domain is a two-dimensional  $(x, z)$  plane; 2. the background atmosphere is hydrostatically balanced, isothermal with  $T_0 \equiv 273 \text{ K}$ , and horizontally homogeneous; 3. the orographic height  $z_m$  is a single mountain with the shape of a Gaussian bell given by

$$z_m(x) = h e^{-\frac{(x-x_c)^2}{a^2}},$$

where  $x_c$  is the center of the domain in  $x$ -direction. We look at two different cases: a)  $h = 4000$  m; and b)  $h = 7000$  m. Note, that in [ZÄNGL \(2012\)](#), the half width  $a$  is taken to be 2000 m. Since the COSMO model cannot be stably integrated up to 6 hours even with the 4000 m high mountain, we have decided to take a flatter mountain by setting  $a = 3000$  m. This choice of  $a$  still causes instabilities for  $h = 7000$  m in the COSMO model, but with its maximum slope of a)  $48.8^\circ$  and b)  $63.4^\circ$  presents a decent test for the two DG dynamical cores.

The domain is  $L = 35$  km wide and  $H = 40$  km high, out of which the upper 15 km form a sponge layer. The time step is 0.01 s for both the finite difference as well as the DG cores. The average distance of the DoFs is 300 m in the horizontal and we choose 100 DoFs in the vertical. The vertical grid size of the elements are computed with the function (2.15) and  $\beta = 0.95$ . The

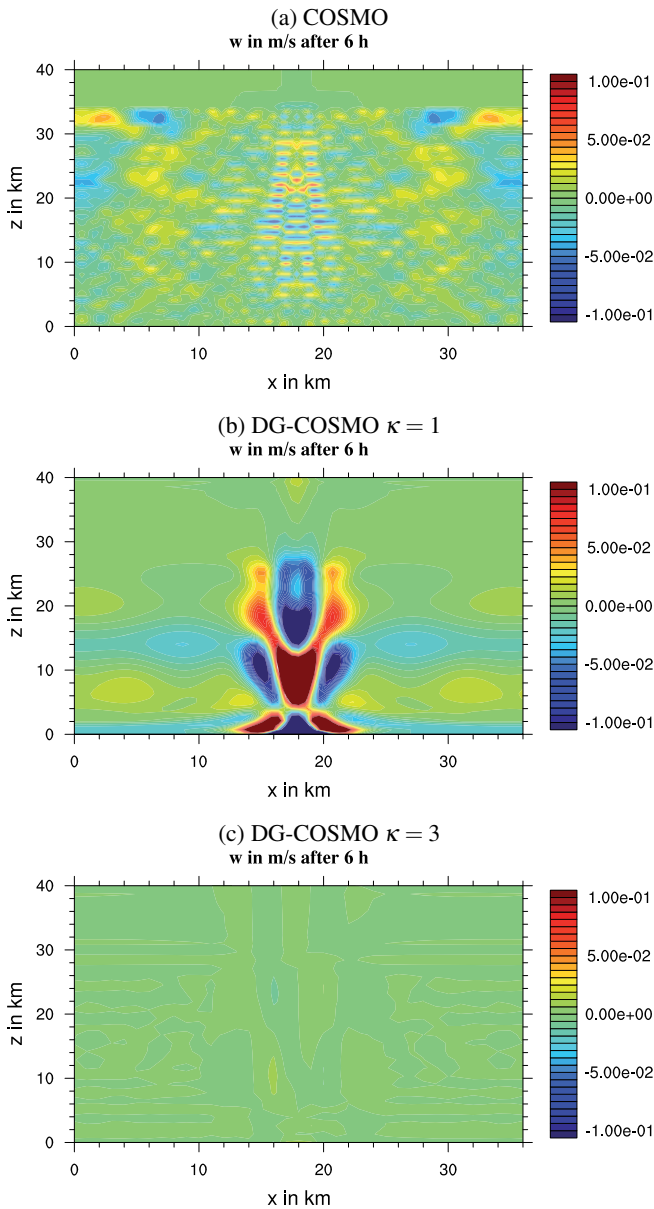


**Figure 5:** Spurious vertical velocity  $w$  of (a) COSMO, (b) DG-COSMO for  $\kappa = 1$ , (c) DG-COSMO for  $\kappa = 3$  for the mountain height  $h = 4000\text{m}$ . The pictures show the grid transformed to the terrain following coordinates, so there is no mountain visible.

COSMO core uses 11 700 DoFs (or grid points). For the DG cores the simulation is repeated for  $\kappa = 1, 2, 3$  for both heights. For all simulations the number of DoFs is chosen to be nearly the same. Fig. 5 shows the spurious vertical velocity after 6 hours. Table 4 lists the grid size and the extrema of the vertical velocity.

The spurious velocity of DG-COSMO for  $\kappa = 2$ , i.e. a third order scheme, is comparable to the extrema of COSMO. For  $\kappa = 3$  the extrema of DG-COSMO are about one order of magnitude smaller than for COSMO. DG-COSMO and COSMO use an explicit sponge layer after each time step to relax their numerical solutions  $\mathbf{q}_{\text{pre}}$  towards the exact (initial) solution  $\mathbf{q}_{\text{init}}$

$$\mathbf{q}_h = (1 - \delta) \mathbf{q}_{\text{pre}} + \delta \mathbf{q}_{\text{init}},$$

**Table 4:** Extrema of spurious vertical velocity in the atmosphere at rest when different numerical models are used. Different polynomial degrees  $\kappa$  are used for DG schemes.

	4 000 m		7 000 m	
	$w_{\text{min}}$	$w_{\text{max}}$	$w_{\text{min}}$	$w_{\text{max}}$
FD-COSMO	$-8.6\text{e-}2$	$7.2\text{e-}2$	unstable	
DG-COSMO $\kappa 1, 67 \times 58$	$-7.1\text{e-}1$	$3.5\text{e-}1$	$-8.5\text{e-}1$	$2.1\text{e-}1$
DG-COSMO $\kappa 2, 48 \times 41$	$-9.5\text{e-}2$	$5.1\text{e-}2$	$-8.5\text{e-}2$	$3.2\text{e-}1$
DG-COSMO $\kappa 3, 37 \times 32$	$-7.7\text{e-}3$	$9.0\text{e-}3$	$-7.4\text{e-}3$	$1.9\text{e-}2$
DUNE $\kappa 1, 67 \times 58$	$-1.3\text{e-}1$	$3.7\text{e-}2$	$-2.0\text{e-}1$	$4.9\text{e-}2$
DUNE $\kappa 2, 48 \times 41$	$-6.1\text{e-}3$	$4.1\text{e-}2$	$-7.6\text{e-}3$	$2.8\text{e-}2$
DUNE $\kappa 3, 37 \times 32$	$-2.3\text{e-}4$	$3.1\text{e-}4$	$-4.8\text{e-}4$	$6.2\text{e-}4$

with the blending function  $\delta(z) = \frac{\alpha}{2} \left( 1 - \cos \left( \pi \frac{z - z_{\text{top}}}{z_{\text{len}}} \right) \right)$ ,  $z_{\text{top}}$  being the top of the computational domain and  $z_{\text{len}}$  the thickness of the sponge layer. For COSMO and DG-COSMO we choose  $\alpha = 0.1$ . On the other hand, the DUNE core relaxes with an additional term in the governing equation. In this way, the relaxed equations (2.14) take the following form

$$\frac{\partial \mathbf{q}}{\partial t} + \nabla \cdot \mathbf{F}(\mathbf{q}) = \mathbf{S}(\mathbf{q}) - \delta(\mathbf{q} - \mathbf{q}_{\text{init}}).$$

Determining the coefficient  $\alpha$  in this context is somewhat less intuitive than in the COSMO/DG-COSMO relaxation. For the extrema values in Table 4, DUNE uses  $\alpha = 80, 75, 50$  for  $\kappa = 1, 2, 3$ , respectively. While not having to cope with the terrain-following metric terms, DUNE does indeed produce smaller spurious velocities only after careful choice of  $\alpha$ , but on the other hand, it proved harder to produce such coefficient for  $\kappa = 2$ . The maximum value for  $\kappa = 2$  in Table 4 is solely due to reflections from the sponge layer. Other than that, the spurious velocities are of one order smaller than in the case of DG-COSMO, whereas for  $\kappa = 1$  are already comparable in the magnitude with the COSMO velocities. We want to mention, that FD-COSMO uses the reference state just to reduce balancing errors stemming mainly from the pressure gradient terms, whereas no explicit means are used to force well-balancing.

### 3.4 Adaptive meshes for cold density current and inertia gravity wave

Different mesh implementations are available in the DUNE package, ranging from fast non adaptive structured meshes to locally adaptive triangular or quadrilateral grids. In order to get an insight of our AMR implementation, we take structured SPGrid from NOLTE (2011), and adaptive ALUGrid from KLÖFKORN (2009), both quadrilateral meshes. Two test cases are considered: 1) cold density current from STRAKA et al. (1993); and 2) inertial gravity wave from SKAMAROCK and KLEMP (1994). The first test case tracks the evolution

of a localised cold current placed in a neutral atmosphere. The bubble current falls to the ground, where no-flux conditions are imposed, and starts to slide along the bottom, developing Kelvin-Helmholtz rotors at its top. The model equations are taken without the  $(\nabla \mathbf{u})^T$ -term in (2.11), which are then identical to the equation set 2 of GIRALDO and RESTELLI (2008). For such equations, a constant viscosity of  $75 \frac{\text{m}^2}{\text{s}}$  is set in order to obtain a grid converged solution which at  $t = 900\text{s}$  is shown in Fig. 6a. This localised flow is an ideal setting for AMR to outperform uniform mesh schemes. The second test case puts somewhat more strain on AMR schemes since the phenomenon spreads across the whole domain. A thermal anomaly centred at  $(x, z) = (100\text{km}, 5\text{km})$  is placed in an atmosphere at rest with the constant Brunt-Väisälä frequency  $N = 0.01 \text{ s}^{-1}$  and a uniform horizontal flow with  $u_0 = 20 \frac{\text{m}}{\text{s}}$ . The potential temperature after  $t = 3000\text{s}$ , is shown in Fig. 6b. We carried out several runs using different resolutions, ensuring that the minimal grid size of the AMR run matches the grid element size of the uniform simulation. For instance, if a uniform simulation uses a 200 m grid resolution, and the AMR run starts with 800 m (denoted “ $\kappa 3$  from 800 m” in Fig. 6e) then we allow the maximal refinement level to be equal to three in the AMR scheme.

In Fig. 6c and Fig. 6d, we can see that the AMR scheme can faithfully represent the correct solutions. In addition, maximal vertical velocity and front position (i.e. position of potential temperature isoline with  $-1\text{K}$ ) have been measured and found to match remarkably well. In terms of  $L_2$ -error versus CPU time, our AMR scheme is around 4 times more efficient than the uniform scheme for the first test cases. On the other hand, the same AMR scheme would refine much of the domain if the flow is expanded with large oscillations in the potential temperature across the whole domain, e.g. shown in Fig. 6d. We can see in Fig. 6f that despite the size of the refinement region in the second test case, the AMR scheme is not considerably less efficient than the uniform scheme. In particular, if we start from a 1 000 m grid resolution using DUNE  $\kappa = 2$  and allow two refinement levels, the AMR scheme will be more efficient by a factor of 1.5. In general, such test cases could be treated, at the cost of accuracy, by adjusting the threshold parameters  $\frac{1}{10}$  and  $\frac{1}{100}$  during the simulation runtime. However, we have not exploited this approach.

### 3.5 Rising moist bubble

To validate the moisture scheme, the setup of the three-dimensional test case described by WEISMAN and KLEMP (1982) was used: the background atmosphere is hydrostatically balanced and described by a vertical profile for the potential temperature  $\theta$  and the relative humidity  $f$

$$\theta(z) = \begin{cases} \theta_{00} + (\theta_{tr} - \theta_{00}) \left(\frac{z}{z_{tr}}\right)^{\frac{5}{4}}, & z \leq z_{tr}, \\ \theta_{tr} e^{\frac{g}{c_p T_{tr}}(z - z_{tr})}, & z > z_{tr}, \end{cases}$$

$$f(z) = \begin{cases} 1 - \frac{3}{4} \left(\frac{z}{z_{tr}}\right)^{\frac{5}{4}}, & z \leq z_{tr}, \\ \frac{1}{4}, & z > z_{tr}, \end{cases}$$

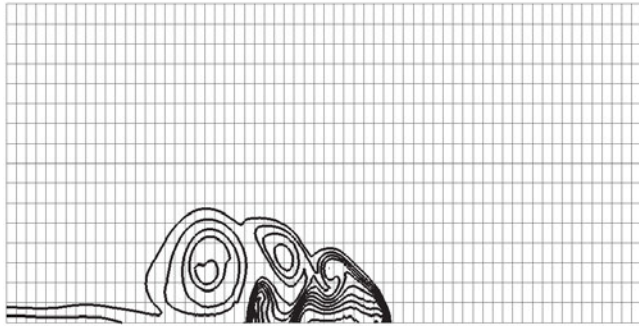
with the potential temperature at the ground equal to  $\theta_{00} = 300\text{K}$  and the troposphere ending at the height  $z_{tr} = 12\text{km}$  with values  $\theta_{tr} = 338\text{K}$  and  $T_{tr} = 213\text{K}$ . The water vapour of the background is clipped to a maximum of 0.014, to simulate a well-mixed boundary layer. The atmosphere is at rest and horizontally homogeneous. This test case is initialised with a perturbation of the temperature given by the following bubble

$$\Delta T = \begin{cases} d_T \cdot \cos\left(\frac{\pi}{2}L\right)^2, & L \leq 1, \\ 0, & L > 1, \end{cases}$$

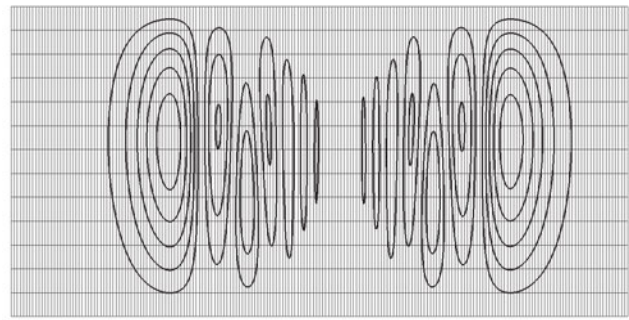
where  $L = \sqrt{\left(\frac{x-x_c}{r_x}\right)^2 + \left(\frac{y-y_c}{r_y}\right)^2 + \left(\frac{z-z_c}{r_z}\right)^2}$ , with  $d_T = 2\text{K}$ ,  $r_x = r_y = 10\text{km}$ ,  $r_z = 1400\text{m}$ . The bubble lies on the ground, i.e.  $z_c = 1400\text{m}$  and  $x_c$  and  $y_c$  denote the horizontal center of the domain. After the start of the simulation, the bubble will rise and due to condensation a cloud will be generated. After a couple of minutes the release of latent heat will accelerate the rising of the cloud until it reaches the top of the troposphere. We compare DG-COSMO at different orders, but with the same effective resolution. Additionally we compare these results to the existing COSMO model at the same resolution to show that they are plausible. At least for the rising period we can expect similar albeit not equal results as this test case is very sensitive. In the original setup there is a turbulence scheme, we simply use a constant diffusion of (2.11)–(2.13) with  $\mu_m = \mu_h = 50\text{m}^2\text{s}^{-1}$ . This results to some extent in a smoother solution which allows a better comparison between COSMO and DG-COSMO. The simulation domain is a box that spans over 50 km in both horizontal directions and over 22 km in the vertical. For the DG scheme the minimal basis was taken for three simulations:  $\kappa = 1$  on  $68 \times 68 \times 54$  elements,  $\kappa = 2$  on  $50 \times 50 \times 40$  elements and  $\kappa = 3$  on  $40 \times 40 \times 32$  elements, so that each has nearly one million DoFs. The COSMO simulation is on the grid  $108 \times 108 \times 86$ . We use for all three DG simulations  $\Delta t = 0.025\text{s}$  and  $\Delta \tau = 3\text{s}$ . COSMO uses the same time step for the dynamics and the saturation adjustment, so we choose 3 s for COSMO.

Fig. 7 compares the vertical velocity of DG-COSMO with  $\kappa = 1, 2, 3$  at 10 min, 15 min, 20 min, which mark the beginning, the middle, and the end of the fast rising. Also the COSMO solution with the same effective resolution as DG-COSMO is shown for comparison. We have compared the cloud water content in Fig. 8 for the same points in time. Because the results strongly depend on the resolution, we bypass the COSMO output routines for these pictures and plot  $(\kappa + 1)^2$  equally spaced points per element in these two figures. In both Fig. 7 and Fig. 8 it can be seen that the case  $\kappa = 1$  is too diffusive. Similar to the well-balanced problem we see that one should use at least  $\kappa = 2$  for a DG scheme similar

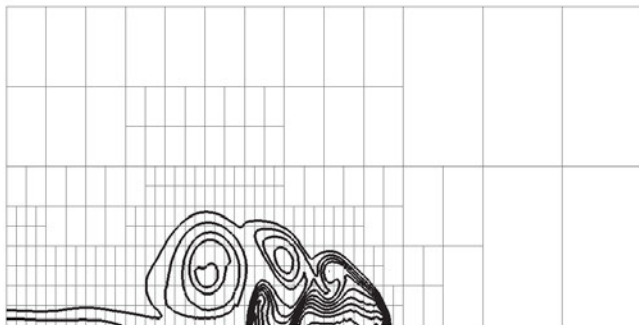
(a) Cold density bubble.  $\theta'$ -isolines at  $-9.5, -8.5, \dots, 0.5$  K on uniform mesh  $64 \times 16$  with DUNE  $\kappa 3$ .



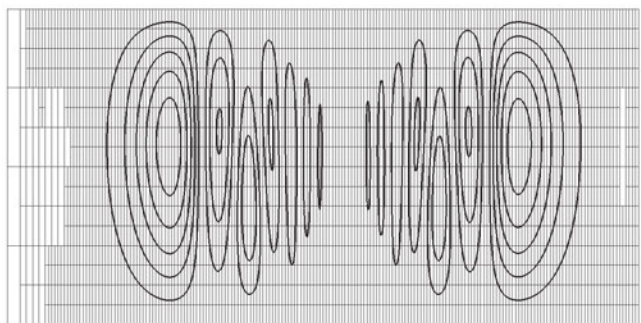
(b) Inertia gravity wave.  $\theta'$ -isolines at  $-0.0015, -0.001, \dots, 0.003$  K on uniform mesh  $200 \times 13$  with DUNE  $\kappa 2$ .



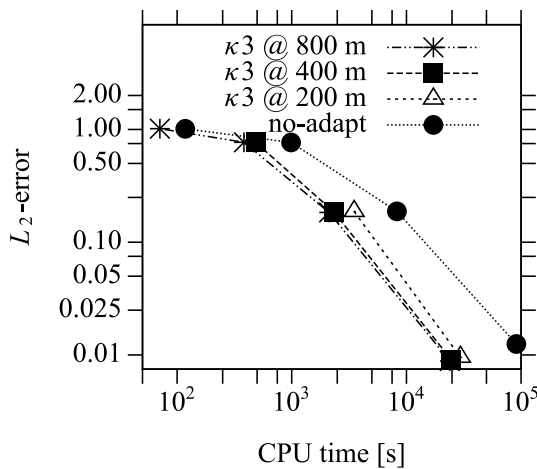
(c) Cold density bubble. Solution on locally adaptive run starting from  $8 \times 2$  DUNE  $\kappa 3$  with the maximal refinement level of 3.



(d) Inertia gravity wave. Solution on locally adaptive run starting from  $25 \times 2$  DUNE  $\kappa 2$  with the maximal refinement level of 3.



(e) Cold density bubble. AMR efficiency.



(f) Inertia gravity waves. AMR efficiency.

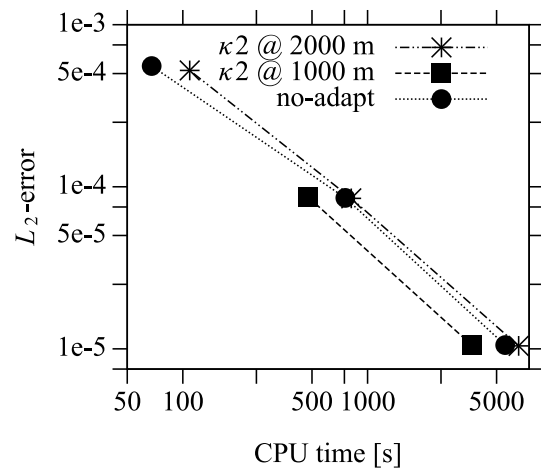


**Figure 6:** Numerical solutions and the corresponding grids at  $t = 3000$  s and  $t = 900$  s of the inertia gravity and the cold density current test case, respectively. First, the simulations on uniform non-adaptive grids with (e) 400 m, 200 m, 100 m, and 50 m; and (f) 1000 m, 500 m, and 250 m  $x$ -resolutions are plotted w.r.t. the CPU time and the  $L_2$ -error. Vertical grid resolution is the same as  $x$ -resolution for the cold density current and twice as small for the inertial gravity test case. In addition, the adaptive runs are added at the corresponding resolutions using different refinement levels  $\lambda$  and initial uniform grids  $x$ -resolutions (given after '@'), i.e. on (e) 400 m ( $\kappa 3 @ 800$  m,  $\lambda = 1$ ), 200 m ( $\kappa 3 @ 800$  m,  $\lambda = 2$ ), ( $\kappa 3 @ 400$  m,  $\lambda = 1$ ), 100 m ( $\kappa 3 @ 800$  m,  $\lambda = 3$ ), ( $\kappa 3 @ 400$  m,  $\lambda = 2$ ), ( $\kappa 3 @ 200$  m,  $\lambda = 1$ ), and 50 m ( $\kappa 3 @ 800$  m,  $\lambda = 4$ ), ( $\kappa 3 @ 400$  m,  $\lambda = 3$ ), ( $\kappa 3 @ 200$  m,  $\lambda = 2$ ); and similarly, on (f) 1000 m ( $\kappa 2 @ 2000$  m,  $\lambda = 1$ ), 500 m ( $\kappa 2 @ 2000$  m,  $\lambda = 2$ ), ( $\kappa 2 @ 1000$  m,  $\lambda = 1$ ), and 250 m ( $\kappa 2 @ 2000$  m,  $\lambda = 3$ ), ( $\kappa 2 @ 1000$  m,  $\lambda = 2$ ). The  $L_2$ -error is computed using (3.1) w.r.t. the elements with the midpoints (e)  $(125\xi, 1200)$  m,  $\xi = 0, \dots, 120$ ; (f)  $(1000 \cdot \xi, 5000)$  m,  $\xi = 0, \dots, 300$ .

to ours. For  $\kappa = 2$  the shape of the cloud is very similar to the cloud of COSMO. But at the top of the cloud there is a larger maximum of  $q_c$ . For  $\kappa = 3$  the correspondence of the big rotor at the right and the left part

of the cloud increases, but the top of the cloud seems to rise faster and additional turbulence appears in the DG-COSMO solution. Fig. 9 shows the development of the maximum and minimum vertical velocity and the

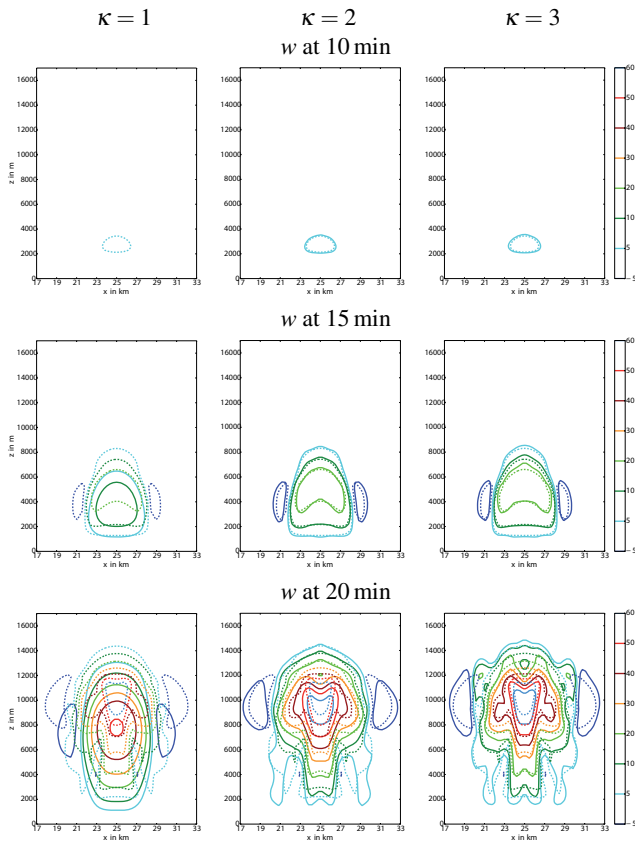


**Figure 7:** Vertical cross section of  $w$  at  $y = 25$  km for the beginning, in the middle and at the end of the fast rising bubble. From left to right is depicted the solution of DG-COSMO for  $\kappa = 1$ ,  $\kappa = 2$  and  $\kappa = 3$  with solid lines. The solution of COSMO is depicted with dashed lines.

maximum of cloud water content of COSMO and DG-COSMO for  $\kappa = 1, 2, 3$ . Here, the case  $\kappa = 1$  looks very smooth compared to COSMO and to  $\kappa = 2, 3$ . While the extrema of the vertical wind velocity are closely comparable for DG-COSMO and COSMO during the rising period of the cloud (first 20 min), the maximum water content is significantly higher for the DG-COSMO solution during this period. This is due to less diffusion of the DG scheme, so the extrema are not smeared out. The COSMO develops after 22 min a strong but local downdraft at the top of the cloud (not shown), which results in values of  $w_{\min}$  down to  $90 \text{ ms}^{-1}$ . This value seems to be unphysically high. In the DG-COSMO solution the downdraft at the same position is much weaker.

The solution is highly dependent on the grid size for both models (not shown), but for the DG solution it also depends on the number of time steps  $\sigma$  between two saturation adjustments. We show an example of this in Fig. 10, where the saturation adjustment is called every 3 s ( $\sigma = 120$ ) on the left side, this is the same time step as in COSMO and each DG time step, i.e. every 0.025 s ( $\sigma = 1$ ) on the right side. For  $\sigma = 1$  two rotors develop symmetrically to the bubble in the lower part of the atmosphere and the top of the bubble is higher. The time of the appearance and the size of these rotors depend

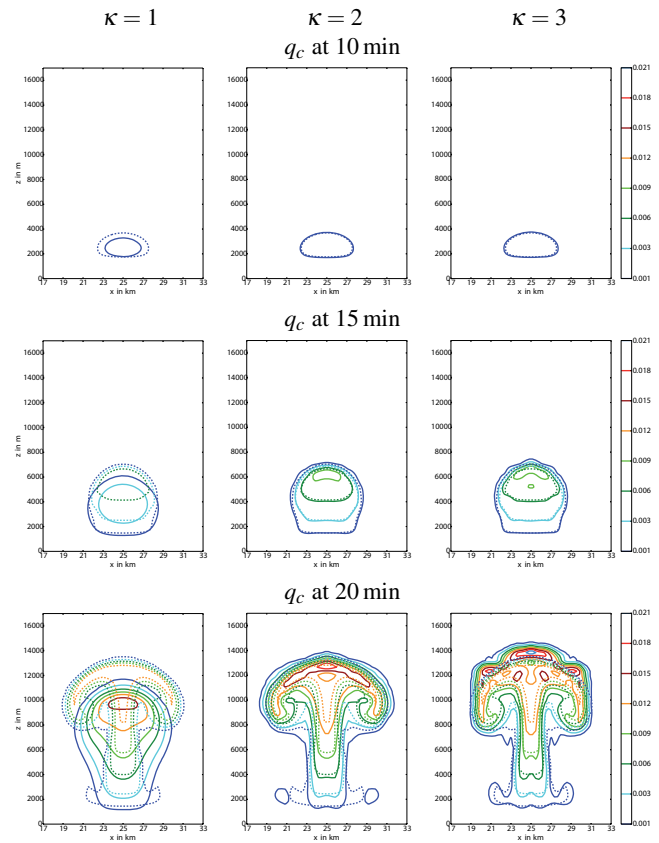


**Figure 8:** Vertical cross section of  $q_c$  at  $y = 25$  km for the beginning, in the middle and at the end of the fast rising bubble. From left to right is depicted the solution of DG-COSMO (solid lines) for  $\kappa = 1$ ,  $\kappa = 2$  and  $\kappa = 3$ . For comparison the solution of COSMO is depicted with dashed lines.

not only on the resolution but also on the size of the parameter  $\sigma$ . Low saturation-adjustment frequency  $\frac{1}{\sigma}$  extents oversaturation so much that the overall convection is slowed down. We have observed similar behaviour for corresponding saturation time-scale values in DUNE (see BRDAR (2012)). Note that the DUNE time-scale value  $s_{v,0}$  (eq. (2.15), pg. 21 in BRDAR (2012)) could be compared to the one of DG-COSMO as  $s_{v,0} \approx \sigma \Delta t$ .

## 4 Conclusion

This article documents the first steps of bringing discontinuous Galerkin (DG) schemes into meteorological applications beyond idealised test cases. To this purpose, we have taken the COSMO model, which is operationally used for numerical weather prediction (NWP) and climate simulations, and have implemented a new dynamical DG core. The choice of the polynomial degree needed to get a suitable approximation for NWP purposes has been discussed. To get a well resolved cloud formation we suggest a polynomial degree  $\kappa \geq 2$  and to mitigate the error of the well-balancing problem we suggest  $\kappa \geq 3$ . So in our opinion the polynomial degree should be at least 3. Otherwise, it has been shown

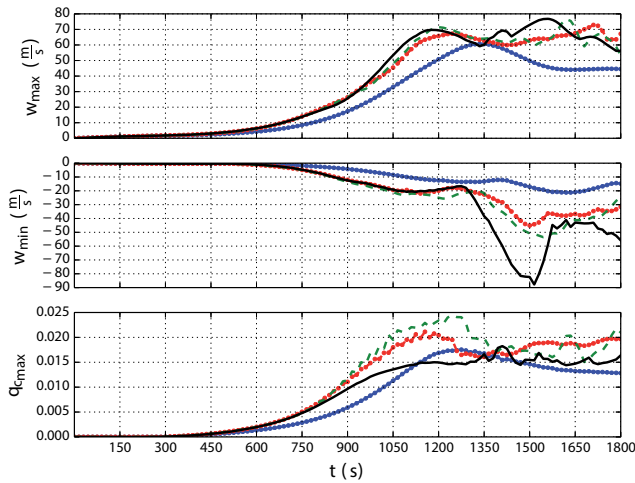


**Figure 9:** Comparison of DG-COSMO  $\kappa = 1$  (blue solid line with dots), DG-COSMO  $\kappa = 2$  (red dashed line with dots), DG-COSMO  $\kappa = 3$  (green dashed line) and COSMO (black solid line) of the evolution of minimum and maximum of the vertical velocity and of the maximum of the cloud water content.

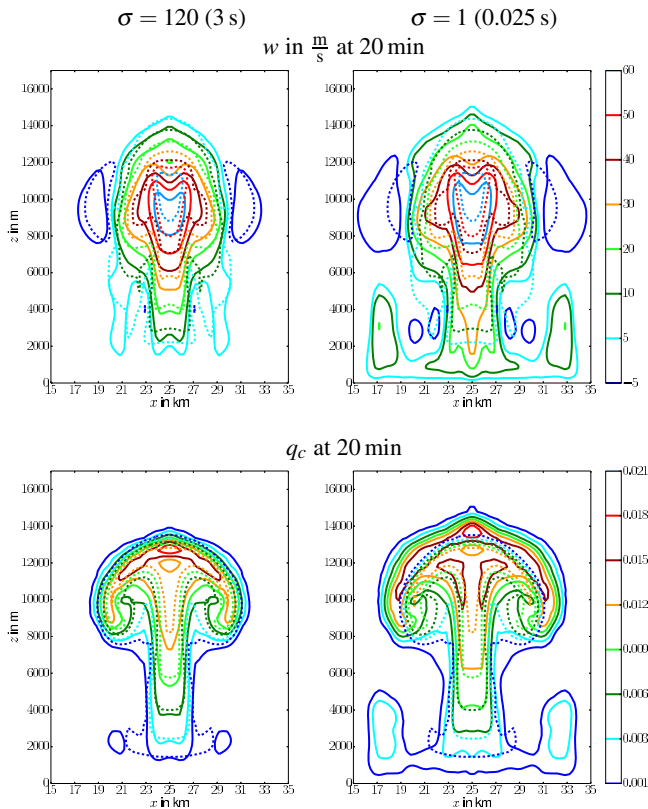


**Figure 10:** Cross section cut in the middle of the domain for the moist rising bubble simulated with DG-COSMO ( $\kappa = 2$ ) for two different values of  $\sigma$  in the process splitting.

in (BALDAUF (2013b)) that for 1-dimensional, linear wave expansion the numerical dispersion relation tends to achieve increasingly higher frequencies compared to the true one with increasing polynomial degree. Consequently, the maximum Courant number decreases faster than  $\sim \frac{1}{\kappa}$ . Since DG methods generally suffer from rela-

tively strong time step restrictions we conclude that the polynomial degree should not be much higher than 3, to reduce computational overhead.

Based on some idealised simulations, we have demonstrated the convergence and functionality of the new core. In particular, we found DG-COSMO is more stable and accurate than COSMO for steep mountain overflow. There is an additional improvement possible by using unstructured grids, which we have demonstrated using the DUNE core. Moreover, DG-COSMO can be improved by using primal DG formulation as in BRDAR et al. (2012), thus eliminating additional variable in the LDG approach, effectively reducing runtime and memory requirement and shrinking the stencil size.

Of course there are still a lot of features missing in DG-COSMO for a realistic weather prediction system. These are mainly the coupling of the physics beside the saturation adjustment and an at least vertically implicit time integration scheme to improve efficiency. The integration of this core within the whole COSMO framework will facilitate the use of the available parametrisations and data assimilation tools used within the operational code COSMO in the next steps.

## Acknowledgments

D.S. and S.B. gratefully acknowledge the support of the German Research Foundation (DFG) under the priority program 1276 MetStröm ‘Multiple Scales in Fluid Mechanics and Meteorology’ with keywords ‘Adaptive numerics for multiscale phenomena’. We thank our colleague ULRICH BLAHAK at Deutscher Wetterdienst for fruitful discussions.

## A The strong conservation form of the budget equations

In this section, we derive the Euler equations in a spherical and terrain following coordinate system  $K'$ . The advantage is, that the transformed grid is Cartesian. Therefore, the grid is structured, without the need of a 3D-triangulation, and the elements are cuboids, for which a simple tensor product of basis polynomials can be used for the DG method. For the following derivations we refer to text books about tensor analysis (e.g. STEPHANI (1988)).

### Scalar case

A general balance equation for a scalar quantity  $\psi(r, t)$  for an arbitrary coordinate system reads in tensorial notation

$$\frac{\partial \psi}{\partial t} + \nabla_k f^k = S \tag{A.1}$$

with a flux  $f$ , a possible source term  $S$  ( $S = 0$  for conserved variables), and with the covariant derivative

$$\nabla_k f^k = \frac{\partial f^k}{\partial x^k} + \Gamma_{kj}^k f^j. \quad (\text{A.2})$$

In this section the Einstein summation rule over equal upper and lower indices is used.  $\Gamma_{ij}^k$  denotes the Christoffel symbol of 2nd kind. It can be expressed by derivatives of the metric tensor  $g_{ij}$ . In particular the property

$$\Gamma_{kj}^k = \frac{1}{\sqrt{G}} \frac{\partial \sqrt{G}}{\partial x^j} \quad (\text{A.3})$$

holds, with  $G := \det g_{ij}$ . Since the coordinate transformation used in COSMO is independent of time, the same holds for  $g_{ij}$  and eq. (A.1) can be written as

$$\frac{\partial \sqrt{G} \psi}{\partial t} + \frac{\partial \sqrt{G} f^k}{\partial x^k} = \sqrt{G} S. \quad (\text{A.4})$$

Note, that the terms containing partial derivatives look like a 'quasi-Cartesian' divergence of a flux and therefore can be discretised in a conserving manner by any finite-volume or DG scheme on a quadrilateral grid. The final formulation using physical components is given in the next section.

### Vector case

The case of the balance equation for the momentum  $\rho u$  with the momentum flux tensor

$$T^{ij} = \rho u^i u^j + g^{ij} p \quad (\text{A.5})$$

and source terms  $S$  reads

$$\frac{\partial \rho u^i}{\partial t} + \nabla_k T^{ik} = S^i. \quad (\text{A.6})$$

By use of (A.3) the covariant derivative of a 2nd stage tensor is

$$\nabla_k T^{ik} = \frac{1}{\sqrt{G}} \frac{\partial \sqrt{G} T^{ik}}{\partial x^k} + \Gamma_{lk}^i T^{lk}. \quad (\text{A.7})$$

Therefore the balance equation can be written as

$$\frac{\partial \sqrt{G'} \rho u^{i'}}{\partial t} + \frac{\partial \sqrt{G'} T^{i'j'}}{\partial x^{j'}} + \sqrt{G'} \Gamma_{l'j'}^{i'} T^{l'j'} = \sqrt{G'} S^{i'}. \quad (\text{A.8})$$

Here we have added upper apostrophes to express all variables in a coordinate system  $K'$  (hence, the denotation ' $'$ ' has a different meaning here than in section 2). The disadvantage of this form is, that the flux term of the momentum flux tensor  $T^{ij}$  is split up and one part must be put into the source term on the rhs. Therefore momentum conservation could be violated numerically. This disadvantage can be reduced by the use of the 'strong conservation' form of the equations (JORGENSEN (2003);

WEDI and SMOLARKIEWICZ (2003)). The basic idea is to keep the derivatives of an arbitrary coordinate system  $K'$  while choosing normalised base vectors of an at least orthogonal coordinate system  $K$  (here: spherical coordinates), i.e. using the physical components of tensors.

Let  $A$  denote the transformation between tensor components in  $K$  and  $K'$ :

$$A_{i'}^i = \frac{\partial x^i}{\partial x^{i'}}, \quad A_{i'}^{i'} = \frac{\partial x^{i'}}{\partial x^i}. \quad (\text{A.9})$$

and for any vector holds the relation  $u^{i'} = A_{i'}^i u^i$ . Furthermore, the physical components in the  $K$ -system (denoted with an upper star index  $*$ ) are

$$u^{*i} = \sqrt{g_{(ii)}} u^i.$$

Brackets around indices indicate, that no summation over equal indices is carried out. Inserting this in (A.8) and multiplication with  $A_{i'}^k$  and  $\sqrt{g_{(kk)}}$  results in

$$\begin{aligned} \frac{\partial \sqrt{G'} \rho u^{*k}}{\partial t} + A_{i'}^k \sqrt{g_{(kk)}} \left[ \frac{\partial \sqrt{G'} T^{i'j'}}{\partial x^{j'}} + \sqrt{G'} \Gamma_{l'j'}^{i'} T^{l'j'} \right] \\ = \sqrt{G'} S^{*k}. \end{aligned} \quad (\text{A.10})$$

The term in square brackets can be partially integrated resulting in:

$$\begin{aligned} \frac{\partial \sqrt{G'} \rho u^{*k}}{\partial t} + \frac{\partial}{\partial x_{j'}} \left( \sqrt{G'} \sqrt{g_{(kk)}} A_{i'}^k T^{i'j'} \right) + \sqrt{G'} b^{*k} \\ = \sqrt{G'} S^{*k} \end{aligned} \quad (\text{A.11})$$

with

$$b^{*k} := -T^{i'j'} \frac{\partial}{\partial x_{j'}} \left( \sqrt{g_{(kk)}} A_{i'}^k \right) + \sqrt{g_{(kk)}} A_{i'}^k \Gamma_{l'j'}^{i'} T^{l'j'}. \quad (\text{A.12})$$

The term  $b^{*k}$  contains all the metric correction terms, which can not be written in form of a 'quasi-Cartesian divergence'. The momentum equation (A.11) can alternatively be expressed by using the physical components of the momentum flux tensor in  $K$

$$\frac{\partial \sqrt{G'} \rho u^{*k}}{\partial t} + \frac{\partial}{\partial x_{j'}} \left( \sqrt{G'} A_{i'}^j \frac{T^{*k*i}}{\sqrt{g_{(ii)}}} \right) = \sqrt{G'} (S^{*k} - b^{*k}). \quad (\text{A.13})$$

We further simplify  $b^{*k}$  by expanding its first summand and by renaming indices of its second summand

$$\begin{aligned} b^{*k} = T^{i'j'} \left[ -A_{i'}^k \frac{\partial}{\partial x_{j'}} \left( \sqrt{g_{(kk)}} \right) - \sqrt{g_{(kk)}} \frac{\partial}{\partial x_{j'}} \left( A_{i'}^k \right) \right. \\ \left. + \sqrt{g_{(kk)}} A_{l'}^k \Gamma_{i'j'}^{l'} \right]. \end{aligned} \quad (\text{A.14})$$

The expression

$$\frac{\partial}{\partial x_{j'}} \left( \sqrt{g^{(kk)}} \right) = A_{j'}^l \frac{\partial}{\partial x_l} \left( \sqrt{g^{(kk)}} \right) = A_{j'}^l \frac{g^{(k)p}}{\sqrt{g^{(kk)}}} \Gamma_{(k)l}^p, \tag{A.15}$$

further simplifies for an orthogonal coordinate system  $K$  by

$$\frac{g^{(k)p}}{g^{(kk)}} = g^{(k)p} \cdot g^{(kk)} = \delta_p^{(k)} \tag{A.16}$$

to

$$\frac{\partial}{\partial x_{j'}} \left( \sqrt{g^{(kk)}} \right) = A_{j'}^l \sqrt{g^{(kk)}} \Gamma_{(k)l}^{(k)}. \tag{A.17}$$

By the transformation properties of the Christoffel symbols one gets

$$\begin{aligned} b^{*k} &= T^{i'j'} \left[ -A_{i'}^k A_{j'}^l \sqrt{g^{(kk)}} \Gamma_{(k)l}^{(k)} - \sqrt{g^{(kk)}} \frac{\partial}{\partial x_{j'}} A_{i'}^k \right. \\ &\quad \left. + \sqrt{g^{(kk)}} A_{i'}^k \left( A_l^i A_{j'}^j \Gamma_{ij}^l + A_m^i \frac{\partial}{\partial x_{j'}} A_{i'}^m \right) \right] \\ &= T^{i'j'} \sqrt{g^{(kk)}} \left[ -A_{i'}^k A_{j'}^l \Gamma_{(k)l}^{(k)} + A_{i'}^i A_{j'}^j \Gamma_{ij}^k \right] \\ &= \sqrt{g^{(kk)}} \left[ -T^{kl} \Gamma_{(k)l}^{(k)} + T^{ij} \Gamma_{ij}^k \right]. \end{aligned} \tag{A.18}$$

Finally using physical components results in the relatively symmetric expression

$$b^{*k} = T^{*i*j} \frac{\sqrt{g^{(kk)}}}{\sqrt{g^{(ii)}} \sqrt{g^{(jj)}}} \Gamma_{ij}^k - T^{*k*j} \frac{1}{\sqrt{g^{(jj)}}} \Gamma_{(k)j}^{(k)}. \tag{A.19}$$

Though  $b^{*k}$  is zero if  $K$  is a Cartesian coordinate system (s. JORGENSEN (2003)), it does not vanish for arbitrary orthogonal coordinate systems. However,  $b^{*k}$  does not contain any properties of  $K'$ , i.e. no contributions from terrain following coordinates. Therefore,  $b^{*k}$  at most depends on curvature contributions of the sphere and consequently these correction terms for momentum can be expected to be very small on the earth. Now, we specialise the former considerations to the spherical coordinate system  $K$ , with the coordinates  $x^i = (\lambda, \phi, z)$  (with  $r = R + z$ ), i.e. we need

$$g_{jk} = \begin{pmatrix} r^2 \cos^2 \phi & 0 & 0 \\ 0 & r^2 & 0 \\ 0 & 0 & 1 \end{pmatrix}, \tag{A.20}$$

and a spherical, terrain-following coordinate system  $K'$ , with the coordinates  $x^{i'} = (\lambda, \phi, \zeta = \zeta(\lambda, \phi, z))$ , for which we need

$$\sqrt{G'} = r^2 \cos \phi \frac{\partial z}{\partial \zeta}, \tag{A.21}$$

$$\frac{\partial x^{i'}}{\partial x^i} = \begin{pmatrix} 1 & 0 & 0 \\ 0 & 1 & 0 \\ \frac{\partial \zeta}{\partial \lambda} & \frac{\partial \zeta}{\partial \phi} & \frac{\partial \zeta}{\partial z} \end{pmatrix}. \tag{A.22}$$

For the physical components of the velocity in  $K$  we use the usual denotations  $u^{*\lambda} \equiv u$ ,  $u^{*\phi} \equiv v$ , and  $u^{*z} \equiv w$ . The physical components of the momentum flux tensor in  $K$  are

$$\begin{aligned} T^{*\lambda*\lambda} &= \rho u^2 + p, \\ T^{*\lambda*\phi} &= T^{*\phi*\lambda} = \rho uv, \\ T^{*\lambda*z} &= T^{*z*\lambda} = \rho uw, \\ T^{*\phi*\phi} &= \rho v^2 + p, \\ T^{*\phi*z} &= T^{*z*\phi} = \rho vw, \\ T^{*z*z} &= \rho w^2 + p. \end{aligned}$$

This finally results in the momentum equations (2.5)–(2.7).

Analogously, we get for the scalar equation (A.4) the form

$$\begin{aligned} \frac{\partial \sqrt{G'} \psi}{\partial t} + \frac{\partial}{\partial \lambda} \left( \sqrt{G'} \frac{f^{*\lambda}}{r \cos \phi} \right) + \frac{\partial}{\partial \phi} \left( \sqrt{G'} \frac{f^{*\phi}}{r} \right) \\ + \frac{\partial}{\partial \zeta} \left( \sqrt{G'} \left( \frac{\partial \zeta}{\partial \lambda} \frac{f^{*\lambda}}{r \cos \phi} + \frac{\partial \zeta}{\partial \phi} \frac{f^{*\phi}}{r} + \frac{\partial \zeta}{\partial z} f^{*z} \right) \right) \\ = \sqrt{G'} S. \end{aligned} \tag{A.23}$$

E.g. for the continuity equation we have  $\psi = \rho$ , with the physical components for the flux  $f$  (i.e. in the spherical coordinate system  $K$ )  $f^{*\lambda} = \rho u$ ,  $f^{*\phi} = \rho v$ ,  $f^{*z} = \rho w$  and  $S = 0$ .

## References

BACON, D.P., N.N. AHMAD, Z. BOYBEYI, T.J. DUNN, M.S. HALL, P.C.S. LEE, R.A. SARMA, M.D. TURNER, 1999: A dynamically adapting weather and dispersion model: the operational multiscale environment model with grid adaptivity (omega). – Mon. Wea. Rev. **128**, 2044–2076.

BALDAUF, M., 2005: The Coordinate Transformations of the 3-Dimensional Turbulent Diffusion in LMK. – COSMO-Newsletter **5**, 132–140, <http://www.cosmo-model.org/content/model/documentation/newsLetters/>.

BALDAUF, M., 2013a: A new fast-waves solver for the runge-kutta dynamical core. – Technical Report **21**, Consortium for Small-Scale Modelling, <http://www.cosmo-model.org/>.

BALDAUF, M., 2013b: The COSMO model: towards cloud-resolving NWP. – In: ECMWF Annual Seminar Proceedings: Recent Developments in Numerical Aspects for Atmosphere and Ocean Modelling. – [www.ecmwf.int](http://www.ecmwf.int).

BALDAUF, M., S. BRDAR, 2013: An analytic solution for linear gravity waves in a channel as a test for numerical models using the non-hydrostatic, compressible Euler equations. – Quart. J. Roy. Meteor. Soc. **139**, 1977–1989, DOI:10.1002/qj.2105.

BALDAUF, M., A. SEIFERT, J. FÖRSTNER, D. MAJEWSKI, M. RASCHENDORFER, T. REINHARDT, 2011: Operational convective-scale numerical weather prediction with the COSMO model: Description and sensitivities. – Mon. Wea. Rev. **139**, 3887–3905.

BEHRENS, J., 2006: Adaptive atmospheric modeling: key techniques in grid generation, data structures, and numerical operations with applications – Springer.

- BLAISE, S., A. ST-CYR, 2012: A Dynamic hp-Adaptive Discontinuous Galerkin Method for Shallow-Water Flows on the Sphere with Application to a Global Tsunami Simulation. – *Mon. Wea. Rev.* **140**, 978–996.
- BOYBEYI, Z., N. AHMAD, D.P. BACON, J. DUNN, M.S. HALL, P.C.S. LEE, R.A. SARMA, 2001: Evaluation of the operational multiscale environment model with grid adaptivity against the european tracer experiment. – *J. Applied Meteo.* **40**, 1541–1558.
- BRDAR, S., 2012: High Order Locally Adaptive Discontinuous Galerkin Approach for Atmospheric Simulations. – Ph.D. thesis, Albert-Ludwigs-Universität Freiburg.
- BRDAR, S., A. DEDNER, R. KLÖFKORN, 2012: Compact and stable discontinuous Galerkin methods for convection-diffusion problems. – *SIAM J. Sci. Comput.* **34**, 263–282.
- BRDAR, S., M. BALDAUF, A. DEDNER, R. KLÖFKORN, 2013: Comparison of dynamical cores for NWP models. – *Theor. Comput. Fluid Dynam.* **27**, 453–472.
- BRYAN, G., J.M. FRITSCH, 2002: A benchmark simulation for moist nonhydrostatic numerical models. – *Mon. Wea. Rev.* **130**, 2917–2928.
- COCKBURN, B., C.-W. SHU, 1989: TVB Runge-Kutta Local Projection Discontinuous Galerkin Finite Element Method for Conservation Laws II: General Framework. – *Math. Comput.* **52**(186), 411–435.
- COCKBURN, B., C.-W. SHU, 1998: The local discontinuous Galerkin method for time-dependent convection-diffusion systems. – *SIAM J. Numer. Anal.* **35**, 2440–2463.
- COCKBURN, B., S.-Y. LIN, C.-W. SHU, 1989: TVB Runge-Kutta Local Projection Discontinuous Galerkin Finite Element Method for Conservation Laws III: One-Dimensional Systems. – *J. Comput. Phys.* **84**, 90–113.
- COCKBURN, B., S. HOU, C.-W. SHU, 1990: The Runge-Kutta local projection Galerkin finite element method for conservation laws IV: The multidimensional case. – *Math. Comp.* **54**, 545–581.
- DEDNER, A., R. KLÖFKORN, M. NOLTE, M. OHLBERGER, 2010: A generic interface for parallel and adaptive scientific computing: Abstraction principles and the DUNE-FEM module. – *Computing* **90**, 165–196.
- DOMS, G., U. SCHÄTTLER, M. BALDAUF, 2011a: A Description of the nonhydrostatic regional COSMO-model, part I: Dynamics and numerics. – Technical report, Consortium for Small-Scale Modelling.
- DOMS, G., J. FÖRSTNER, E. HEISE, H.-J. HERZOG, D. MIRONOV, M. RASCHENDORFER, T. REINHARD, B. RITTER, R. SCHRODIN, J.-P. SCHULZ, G. VOGEL, 2011b: A Description of the nonhydrostatic regional COSMO-model, part II: Physical parameterization. – Technical report, Consortium for Small-Scale Modelling.
- DURRAN, D., J.B. KLEMP, 1983: A compressible model for the simulation of moist mountain waves. – *Mon. Wea. Rev.* **111**, 2341–2361.
- GABERŠEK, S., F.X. GIRALDO, J. DOYLE, 2012: Dry and moist idealized experiments with a two-dimensional spectral element model. – *Mon. Wea. Rev.* **140**, 3163–3182.
- GASSNER, G., 2009: Discontinuous Galerkin Methods for the Unsteady Compressible Navier-Stokes Equations. – Ph.D. thesis, Aerospace Engineering and Geodesy of the University of Stuttgart.
- GIRALDO, F.X., M. RESTELLI, 2008: A study of spectral element and discontinuous Galerkin methods for the Navier-Stokes equations in nonhydrostatic mesoscale atmospheric modeling: Equation sets and test cases. – *J. Comp. Phys.* **227**, 3849–3877.
- GIRALDO, F.X., J.S. HESTHAVEN, T. WARBURTON, 2002: Nodal high-order discontinuous Galerkin methods for the spherical shallow water equations. – *J. Comput. Phys.* **181**, 499–525.
- GOPALAKRISHNAN, S.G., D.P. BACON, N.N. AHMAD, Z. BOYBEYI, J. DUNN, THOMAS, M.S. HALL, Y. JIN, C.S. LEE, PIUS, D.E. MAYS, R.V. MADALA, A. SARMA, M.D. TURNER, T.R. WAIT, 2002: An operational multiscale hurricane forecasting system. – *Mon. Wea. Rev.* **130**, 1830–1847.
- HALL, D.M., R.D. NAIR, 2012: Discontinuous Galerkin Transport on the Spherical Yin–Yang Overset Mesh. – *Mon. Wea. Rev.* **141**, 264–282.
- JABLONOWSKI, C., R. OEHMKE, Q. STOUT, 2009: Block-structured adaptive meshes and reduced grids for atmospheric general circulation models. – *Phil. Trans. R. Soc. A* **367**, 4497–4522.
- JØRGENSEN, B.H., 2003: Tensor formulation of the model equations on strong conservation form for an incompressible flow in general coordinates. – Technical report, Riso National Laboratory, Roskilde, Denmark.
- KELLY, J.F., F.X. GIRALDO, 2012: Development of the nonhydrostatic unified model of the atmosphere (NUMA): Limited-area mode. – *J. Computat. Phys.* **231**, 7988–8008.
- KLÖFKORN, R., 2009: Numerics for Evolution Equations. – Ph.D. thesis, Albert-Ludwigs-Universität, Freiburg i. Br.
- MÜLLER, A., J. BEHRENS, F.X. GIRALDO, V. WIRTH, 2013: Comparison between adaptive and uniform discontinuous Galerkin simulations in dry 2D bubble experiments. – *J. Computat. Phys.* **235**, 371–393.
- NAIR, R.D., H.-W. CHOI, H. TUFO, 2009: Computational aspects of a scalable high-order discontinuous Galerkin atmospheric dynamical core. – *Computers Fluids* **38**, 309–319.
- NOLTE, M., 2011: Efficient numerical approximation of the effective Hamiltonian. – Ph.D. thesis, Albert-Ludwigs-Universität Freiburg i. Br.
- SKAMAROCK, W.C., J.B. KLEMP, 1994: Efficiency and accuracy of the Klemp-Wilhelmson time-splitting technique. – *Mon. Wea. Rev.* **122**, 2623–2630.
- SKAMAROCK, W., J. KLEMP, M. DUDA, L. FOWLER, S.-H. PARK, T. RINGLER, 2012: A Multi-scale Nonhydrostatic Atmospheric Model Using Centroidal Voronoi Tessellations and C-Grid Staggering. – *Mon. Wea. Rev.* **240**, 3090–3105.
- STEPHANI, H., 1988: Allgemeine Relativitätstheorie. – Dt. Verlag d. Wiss., Berlin, 280 pp.
- STEPPELER, J., G. DOMS, U. SCHÄTTLER, H. BITZER, A. GASSMANN, U. DAMRATH, G. GREGORIC, 2003: Mesogamma scale forecasts using the nonhydrostatic model LM. – *Meteor. Atmos. Phys.* **82**, 75–96.
- STRAKA, J.M., R.B. WILHELMSON, L.J. WICKER, J.R. ANDERSON, K.K. DROEGEMEIER, 1993: Numerical solutions of a nonlinear density current: A benchmark solution and comparisons. – *Int. J. Num. Meth. Fluids* **17**, 1–22.
- TOMITA, H., 2008: New microphysical schemes with five and six categories by diagnostic generation of cloud ice. – *J. Meteorol. Soc. Japan. Ser. II* **86A**, 121–142.
- WEDI, N.P., P.K. SMOLARKIEWICZ, 2003: Extending Gal-Chen and Somerville terrain-following coordinate transformation on time-dependent curvilinear boundaries. – *J. Comput. Phys.* **193**, 1–20.
- WEISMAN, M.L., J.B. KLEMP, 1982: The dependence of numerically simulated convective storms on vertical wind shear and buoyancy. – *Mon. Wea. Rev.* **110**, 504–520.
- ZÄNGL, G., 2012: Extending the numerical stability limit of terrain-following coordinate models over steep slopes. – *Mon. Wea. Rev.* **140**, 3722–3733.